AUTHOR ACCEPTED MANUSCRIPT: DOI 10.1016/j.quascirev.2024.108866

Resolving the paradox of conflicting glacial chronologies: Reconstructing the pattern of deglaciation of the Magellan cordilleran ice dome (53-54°S) during the Last glacial – interglacial transition.

Robert D. McCulloch[a,b,*], Michael J. Bentley[c], Derek Fabel[d], Hans Fernández-Navarro[e,f], Juan Luis Garcia[f], Andrew S. Hein[a], Carla Huynh[a], Stewart S.R. Jamieson[c], María-Paz Lira[c], Christopher Lüthgens[g], Grace A. Nield[c], Manuel San Román[h], Eileen W. Tisdall[i]

[a] School of Geosciences, The University of Edinburgh, Edinburgh, UK

[b] Centro de Investigación en Ecosistemas de la Patagonia (CIEP), Coyhaique, Aysén, Chile

[c] Department of Geography, University of Durham, South Road, Durham, UK

[d] Scottish Universities Environmental Research Centre, Scottish Enterprise Technology Park, East Kilbride, UK

[e] Instituto de Ciencias Agroalimentarias, Animales y Ambientales (ICA3), Universidad de O'Higgins, San Fernando, Chile

[f] Instituto de Geografía, Facultad de Historia, Geografía y Ciencia Política, Pontificia Universidad Católica de Chile, Santiago, Chile

[g] Institute of Applied Geology, Department of Civil Engineering and Natural Hazards, University of Natural Resources and Life Sciences (BOKU), Vienna, Austria

[h] Instituto de la Patagonia, Universidad de Magallanes, Punta Arenas, Chile

[i] Biological and Environmental Sciences, University of Stirling, Stirling, UK

* Corresponding author: v1rmccul@ed.ac.uk

Abstract

Raised shorelines and associated lacustrine sediments in the central Estrecho de Magallanes (Strait of Magellan) have been interpreted as products of cordilleran glaciers impounding a large proglacial lake and preventing drainage to the South Pacific and Southern Ocean during the Late glacial between c. 15.0 and 12.0 cal ka BP. However, a growing body of glacial geological evidence points towards an earlier retreat of the Magellan cordilleran ice dome, insufficient to dam lakes at that time. We critically re-evaluate the extant evidence for the c. 15.0-12.0 cal ka BP lake, here named 'Lago Kawésqar', and provide further sedimentological and chronological evidence for its existence. We also provide new cosmogenic surface nuclide dating of erratic and bedrock samples collected

Accepted refereed manuscript of: Mcculloch RD, Bentley MJ, Fabel D, Fernández-Navarro H, Garcia JL, Hein AS, Huynh C, Jamieson SSR, Lira M, Lüthgens C, Nield GA, San Román M & Tisdall EW (2024) Resolving the paradox of conflicting glacial chronologies: Reconstructing the pattern of deglaciation of the Magellan cordilleran ice dome (53–54°S) during the last glacial – interglacial transition. *Quaternary Science Reviews*, 344, Art. No.: 108866. https://doi.org/10.1016/j.quascirev.2024.108866

from extensive field campaigns that confirm the rapid and widespread retreat of the Magellan ice fields to the inner fjords of the Fuegian archipelago by c. 16.0 cal ka BP. To resolve the apparent paradox between these two lines of evidence we propose that glacial isostatic adjustment led to a topographic barrier to lake drainage rather than an ice dam. We use Glacial Isostatic Adjustment modelling to demonstrate that rapid isostatic recovery following the early deglaciation after c. 17.0 cal ka BP likely led to elevation of the present shallow south-western coastal margin of the Fuegian archipelago. Final drainage of Lago Kawésqar was probably caused by neotectonic subsidence of the same margin along the boundary of the South American – Scotia tectonic plates at c. 12.0 cal ka BP.

Keywords

Fuego-Patagonia, cosmogenic dating, OSL dating, tephrochronology, lake sediments, glacial isostatic adjustment, neotectonics

1. Introduction

Field-based reconstructions of the Patagonian Ice Sheet (PIS) and the sequence of events during deglaciation after the Last Glacial Maximum (LGM) (25.2-20.3 cal ka BP, McCulloch et al., 2005a) provide important insights into the changing southern hemisphere climate drivers of landscape change during the last glacial – interglacial transition (LGIT). During the LGM the PIS coalesced into a large single ice sheet along the Andean cordillera (38°-55°S) that drained towards the South Pacific Ocean in the west and into large glacially-scoured basins and troughs in the east (Fig. 1a). Multiple studies have sought to reconstruct the extent and timing of Late Quaternary glacier fluctuations within different sectors of the PIS (Davies et al., 2020 and references therein). The topographic configuration of the southern Andes is such that during periods when the Magellan cordilleran ice dome (part of the PIS between 52°-55°S) advanced into the Fuegian channels, drainage to the Pacific and Southern Oceans was blocked and large pro-glacial lakes formed along the eastern flanks of the ice sheet. The ice-dammed lakes drained eastward through meltwater routes to the South Atlantic (Fig. 1b). During retreat of the Magellan cordilleran ice dome the eventual collapse of the ice dams would have resulted in the catastrophic drainage of the pro-glacial lakes followed by the incursion of marine waters as global sea-level rose from the LGM minimum of ~-125 m asl. (Lambeck et al., 2014). The presence and timing of the Magellan pro-glacial lakes also helps constrain the glacial history of the region (Björck et al., 2021).

In the Estrecho de Magallanes (Strait of Magellan) (~53°S), the succession of proglacial lakes has left a suite of extensive glacial lacustrine sediments and associated shorelines, now raised and tilted by

differential isostatic uplift (Fig. 2). These were first mapped by Caldenius (1932) and this work has subsequently been built upon (Auer, 1959; Porter et al., 1984; Clapperton et al., 1995; McCulloch and Bentley, 1998; McCulloch et al., 2005b; Björck et al., 2021). Two distinct Late glacial palaeoshorelines and associated lacustrine sediments have been identified (McCulloch et al., 2005b) (Fig. 2). The higher palaeoshoreline (~30-60 m asl., altitudes are from the central section of the Estrecho de Magallanes) is linked to a pro-glacial lake formed as the Magellan glacier retreated after c. 18.0 cal ka BP (Glacial Stage D of Clapperton et al., 1995, Fig. 1b). The lower lake level was

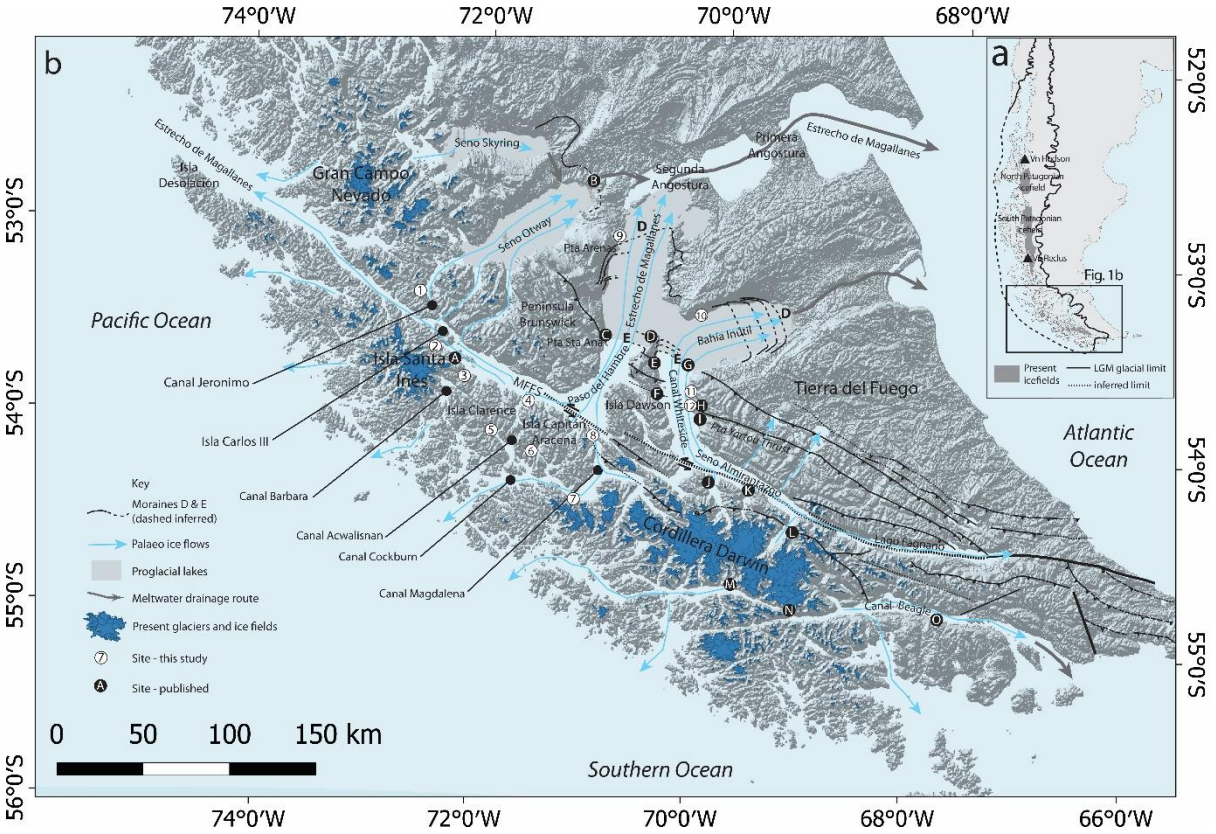

Figure 1: The Estrecho de Magallanes, Fuegian archipelago and present glaciers and ice fields (from Gurdiel et al. (2022): 1 Estero Condor, Canal Jeronimo; 2 Peninsula Ulloa, Isla Santa Inés, 3 Caleta Miller, Isla Cayetano; 4 Seno Pedro, Isla Clarence; 5 Seno Dyneley (E & W), Isla Clarence; 6 Laguna Arcilla, Isla Capitán Aracena; 7 Seno Chico and 8 Puerto Hope, Canals Magdalena - Cockburn; 9 Pampa Alegre, Peninsula Burnswick; 10 Puente Charlie, Bahía Inútil; 11 Río Caleta and 12 Punta Yartou, Canal Whiteside. Published sites: A Lago Ballena (Fontana and Bennett, 2012); B Seno Otway meltwater channel (McCulloch et al., 2005b); C Puerto del Hambre (McCulloch and Davies, 2001); D Cabo Valentín II (McCulloch et al., 2005a); E Río Grande (Mansilla, 2015); F Cerro Fox (Blaikie 2020); G MD07-3132 (Aracena et al., 2015); H Punta Yartou (Mansilla et al., 2016); I Lago Carquito (Moreno et al., 2023); J Punta Esperanza (Hall et al., 2019); K Punta Marinelli (Hall et al., 2013) also JPC67 and JPC77 marine cores, Seno Almirantazgo (Boyd et al., 2008); L Dalla Vedova (Reynhout et al., 2022); M Bahía Pía, N Bahía Holanda (Hall et al., 2013); O Punta Burslem, Canal Beagle (Blaikie 2020). A summary of the Magellan-Fagnano Fault System (MFFS) from Sánchez et al. (2010). The moraine limits of Glacial Stage D the Estrecho de Magallanes and Bahía Inútil (Bentley et al., 2005) and equivalent in Seno Skyring (Lira et al., 2022) and an approximate extent of the proglacial lakes indicated by the Late glacial palaeoshorelines are indicated. The moraine limits of Glacial Stage E in the Estrecho de Magallanes are from McCulloch and Bentley (1998).

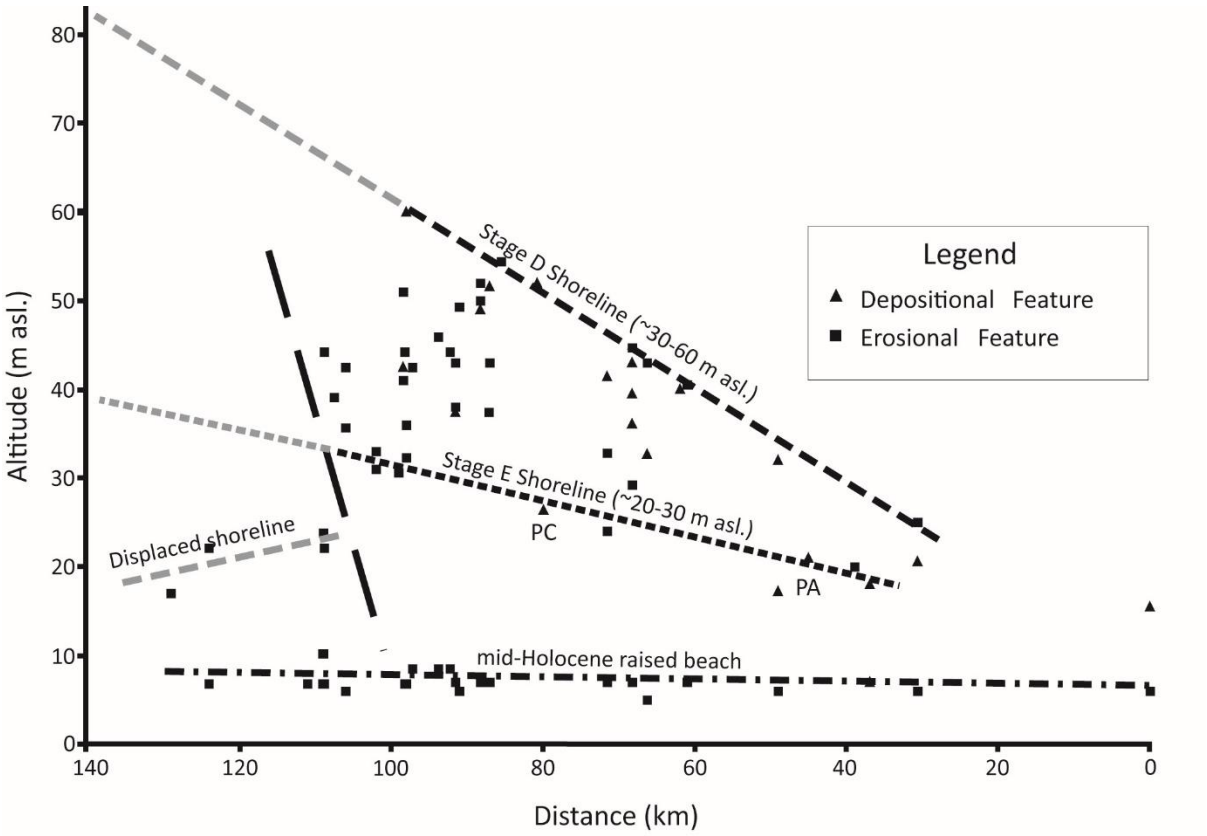

Figure 2. Palaeoshoreline diagram for the Estrecho de Magallanes. The dashed line marks the morphological limit of the Stage D shoreline (c. 30–60 m a.s.l). The points beneath are small erosion notches and shingle ridges that are assumed to be recessional features as the glacial lake lowered and are time transgressive. The short-dash line marks the lowest Stage E shoreline (c. 20–30 m a.s.l) that is identified based on morphometry and by sites linked by the Vn Reclus tephra. The long-dashed line marks the approximate boundary of the down faulting, the slope reflects the north-west to south-east trend of the MFFS. The grey dashed lines extrapolate the lake levels south of the fault boundary. The mid-Holocene raised beach is marked by the dot-dash line c. 6–10 m a.s.l). The distance (in km) on the x-axis is measured from the Segunda Angostura (Fig. 1). PC = Puente Charlie, PA = Pampa Alegre. (From McCulloch et al., 2005a).

identified at ~20 m asl. near Punta Arenas rising to ~30 m asl. along the northern peninsula of Isla Dawson. The 20-30 m asl. shoreline appeared to grade to a moraine limit on the eastern and western sides of the Isla Dawson peninsula, ~80 km north of the present ice margins in the Cordillera Darwin, although it was undated (Glacial Stage E, McCulloch and Bentley, 1998) (Fig. 1b). Near-shore deposits, e.g. beach ridges and deeper water deposits, laminated clays and silts, including drop stones, are geomorphically linked to the ~20-30 m asl. shoreline. In several places such lacustrine deposits overlie a key chronostratigraphic marker provided by the Volcán (Vn) Reclus tephra layer geochemically linked and radiocarbon dated to c. 15.0 cal ka BP at sites around the Magellan region (McCulloch et al., 2005a; Sagredo et al., 2011). At several sites close (~ 1 m asl.) to present sea-level, the Vn Reclus tephra layer has been found within peat layers (i.e. sub-aerial deposits) beneath

bluish-grey lacustrine sediments. Peat deposits immediately above the lacustrine deposits have been radiocarbon dated to c. 12.0 cal ka BP (McCulloch et al., 2005b).

Beneath the ~20-30 m asl palaeoshoreline there is a further continuous raised shoreline at ~6-10 m asl. (Fig. 2). This shoreline is near-horizontal and can be traced along the shores of the Estrecho de Magallanes and Bahía Inútil. Sediments associated with this raised shoreline contain marine shells indicating that the low-lying coastal margins were inundated by rising sea-levels. Marine sediments identified in cores from isolation basins provide ages that suggest the onset of the inundation was c. 9.2 cal ka BP and emergence began at c. 5.0 cal ka BP (Porter et al., 1984; McCulloch and Davies, 2001).

From this evidence, McCulloch et al. (2005b) inferred the following sequence of events: 1) glacier retreat after the Stage D glacier advance and the formation of the 30-60 m asl. proglacial lake in the central Estrecho de Magallanes. Continued retreat of the Stage D glacier from the Fuegian channels led to a collapse of the ice dam and drainage of the 30-60 m asl. pro-glacial lake at c. 16.1 cal ka BP; 2) the formation of sub-aerial deposits close to present sea-level and the deposition of the Vn Reclus tephra layer at c. 15.0 cal ka BP, which implies the Estrecho de Magallanes was open to the Southern Ocean; 3) a readvance (Glacial Stage E) of the Magellan cordilleran ice dome leading to the formation of the 20-30 m asl. pro-glacial lake between c. 15.0 and 12.0 cal ka BP; 4) Glacier retreat and collapse of the ice dam at c. 12.0 cal. ka BP. The rising global sea-level then enabled marine waters from the Pacific and Southern Oceans to enter the Estrecho de Magallanes from the south eventually leading to through-flow between the South Pacific and South Atlantic oceans sometime between c. 10.0 and 9.0 cal ka BP.

The Stage E ice advance, damming the 20-30m asl. lake, would have been broadly contemporary with the Antarctic Cold Reversal (ACR), 14.7-13.0 ka (Pedro et al., 2016). It could suggest that the poleward migration of the southern westerly winds during the LGIT led to rapid retreat in northern Patagonia while feeding a re-advance in southern Patagonia, thus leading to an asymmetrical response of the PIS as the southern hemisphere warmed (McCulloch et al., 2000).

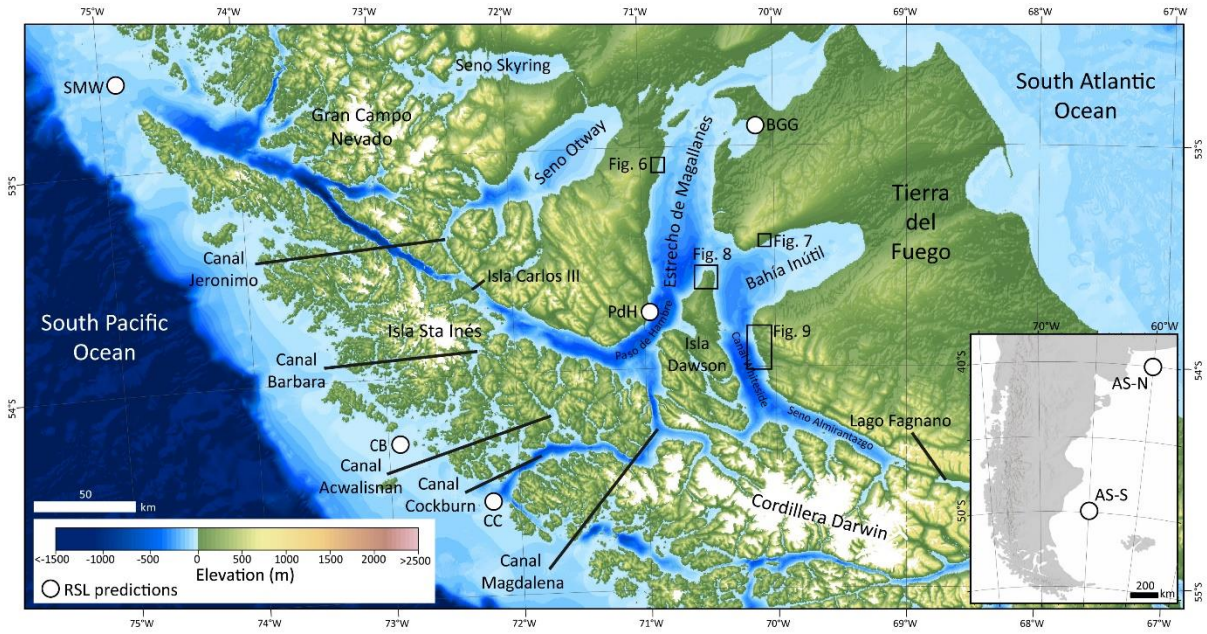

Figure 3. Bathymetry of the southern Magellan region. Source: ETOPO 2022 (NOAA, 2022) . Locations of relative sea level predictions from GIA modelling indicated (see Table 4): a) Inset: Argentine shelf AS-N (north), AS-S (south). Main map b) Pacific shelf: Strait of Magellan west (SMW), Canal Barbara (CB), Canal Cockburn (CC). Central Strait of Magellan: Bahía Gente Grande (BGG), Puerto del Hambre (PdH).

The evidence and interpretation of the Late glacial (Stage E) pro-glacial lake, including implications for the human history of migration onto Tierra del Fuego during the LGIT (Morello et al., 2012), appeared to be firm. The proposed Isla Dawson moraine limit being the ice-dam could be discounted when the Vn Reclus tephra was found further to the south (Mansilla et al., 2016), although an ice-dam somewhere in the Fuegian archipelago was still necessitated by the 20-30 m asl. Stage E raised lake shoreline evidence. However, more recent evidence from the north-eastern fjords of the Cordillera Darwin indicated that glacier retreat to within <18 km of the present ice margins occurred sometime before c. 17.1 cal ka BP (Hall et al., 2017, 2019). Other similar minimum ages for ice retreat have been obtained from the Cordillera Darwin and the Fuegian archipelago (16.0 cal ka BP, Fontana and Bennett, 2012; 17.1 cal ka BP, McCulloch et al., 2020). Also, no evidence has been found for submerged moraines in the southern Magellan channels associated with a Stage E glacier advance (Fernández et al., 2017). This evidence for early and widespread glacier retreat of the Magellan glaciers after the LGM is incompatible with the evidence for a Late glacial readvance and formation of an ice dammed lake at c. 15.0 – 12.0 cal ka BP. Therefore, although the two lines of evidence are robust, they present a paradox. The significant implications of this paradox for our understanding of LGIT climate and landscape change have inspired this multi-proxy project to re-investigate the glacial and landscape history of the Estrecho de Magallanes.

Here we present new stratigraphical and chronological (radiocarbon (^{14}C) and luminescence ages from K-Fs single grains) evidence for the timing of the 20-30 m asl. palaeolake in the central Estrecho de Magallanes. We also provide new cosmogenic ^{10}Be and radiocarbon (^{14}C) ages for the timing of glacier retreat into the Fuegian channels and fjords to the north and west of the Cordillera Darwin. We then offer a paradigm shift, supported by glacial isostatic adjustment (GIA) modelling, to resolve the paradox between the Late glacial lake evidence and the minimum ages for early and widespread glacier retreat after the LGM.

2. Regional Setting

The Magellan region is characterised by the eastward curvature of the southern Andean cordillera with large marine embayments (Seno Skyring, Seno Otway, Bahía Inútil), large marine channels (Estrecho de Magallanes, Canal Beagle), fjords, and the Fuegian archipelago bordering the Southern Ocean. The Estrecho de Magallanes provides passage between the South Pacific and South Atlantic oceans, and the south-west section follows the Magellan-Fagnano Fault System (MFFS) which is an active tectonic boundary between the Scotia and South American plates (Sánchez et al., 2010). The MFFS is expressed as an east-west trough that follows the western arm of the Estrecho de Magallanes to Seno Almirantazgo and eastward to Lago Fagnano (Fig. 1b). To the north of the principal plate boundary there are a series of parallel strike-slip faults with a component of vertical reverse (thrusting) movement trending along the Punta (Pta) Santa Ana – Pta Yartou axis. Movement along this boundary is predominantly left-lateral at a rate of ~5-7 mm a^{-1} (Mendoza et al., 2011). Vertical movements along the MFFS have not been reliably estimated, although Bentley and McCulloch (2005) have suggested a localised postglacial neotectonic displacement of ~30 m. The geology to the south of the MFFS is dominated by the Cordillera Darwin batholith surrounded by Early Cretaceous rocks. To the north of the MFFS the landscape is predominantly formed by Late Cretaceous to Eocene rocks overlain with Quaternary glacial deposits (Sánchez et al., 2010).

Within the Fuegian archipelago there are presently three significant ice fields on the topographic high points of the Gran Campo Nevado, Isla Santa (Sta) Inés and the Cordillera Darwin, here collectively termed the Magellan cordilleran ice fields (Fig. 1b). The islands of the archipelago between Isla Sta Inés and the Cordillera Darwin, principally Isla Clarence and Isla Capitán Aracena, are relatively low-lying. In the central section of the Estrecho de Magallanes the main channel is split into two by Isla Dawson. To the west of Isla Dawson, the Strait continues through Paso del Hambre, turns to the west and occupies the main MFFS boundary. To the east of Isla Dawson lies Canal Whiteside which turns eastward along the line of the MFFS towards Lago Fagnano. The western arm of the Estrecho de Magallanes flows to the South Pacific Ocean through the main channel at Isla

Desolación. The western section of the Estrecho de Magallanes is also open to the Southern Ocean through three smaller channels through the Fuegian archipelago, namely Canal Magdalena, Canal Acwalisnan and Canal Barbara (Fig. 1b).

The bathymetry of the Estrecho de Magallanes is relatively shallow to the north (~-50 m depth) between the Primera and Segunda Angosturas (first and second narrows) which are formed by moraine arcs deposited across the Estrecho de Magallanes (Clapperton et al. 1995; Bentley et al., 2005; Peltier et al., 2021) (Figs. 1b and 3). To the south in Paso del Hambre the Estrecho de Magallanes deepens to ~-550 m and progressively deepens to ~-1000 m towards the Pacific, although there is a shallow sill (~-100 m depth) at Isla Carlos III. Canal Magdalena – Canal Cockburn is a major navigation channel to the south and depths vary between ~-200 and ~-500 m (Instituto Hidrográfico de la Armada de Chile chart 1201). Although there is limited bathymetry for Canals Barbara and Acwalisnan, the former is estimated to be <~-25 m deep and the latter is only navigable in small boats at high tide observed by this study. It should be noted that the Canal Whiteside – Seno Almirantazgo channel is not open to the Southern Ocean.

3. Methods

3.1 ^{10}Be surface exposure dating

3.1.1 ^{10}Be Sample collection

To constrain the onset of deglaciation at Punta Yartou, we measured cosmogenic ^{10}Be concentrations in 16 boulders from moraine ridges preserved east of Canal Whiteside (Fig. 4a). South of the MFFS the region is dominated by the ice scoured landscape of the Fuegian archipelago. Here we adopted a broader approach of sampling 21 erratic boulders (Fig. 4b) and 10 ice-moulded bedrock (Fig. 4c) samples for ^{10}Be dating from low-altitude locations (<300 m asl.; Table 1) along the channels of Canal Jeronimo (the access to Seno Otway), Canal Barbara, Canal Acwalisnan, including the inner fjord of Seno Dyneley, Canal Magdalena and Canal Cockburn to help constrain when the Strait and the channels around Isla Clarence and Isla Capitán Aracena became ice free during the LGIT.

For each site, we collected 2-4 samples, of which ~1 was sampled from bedrock, while the remainder were from erratic boulders perched on bedrock (i.e., in a stable position) at elevations ranging from ~40 – 285 m asl. We selected quartz-rich samples (mostly granodiorite and granite) and collected 1-2 kg of sample from the top and centre of surfaces using an angle grinder, hammer, and chisel. We preferentially sampled large erratic boulders from stable positions on bedrock (or moraine crests), away from potential rock fall sources. Boulders with subangular shapes and evidence of minimal

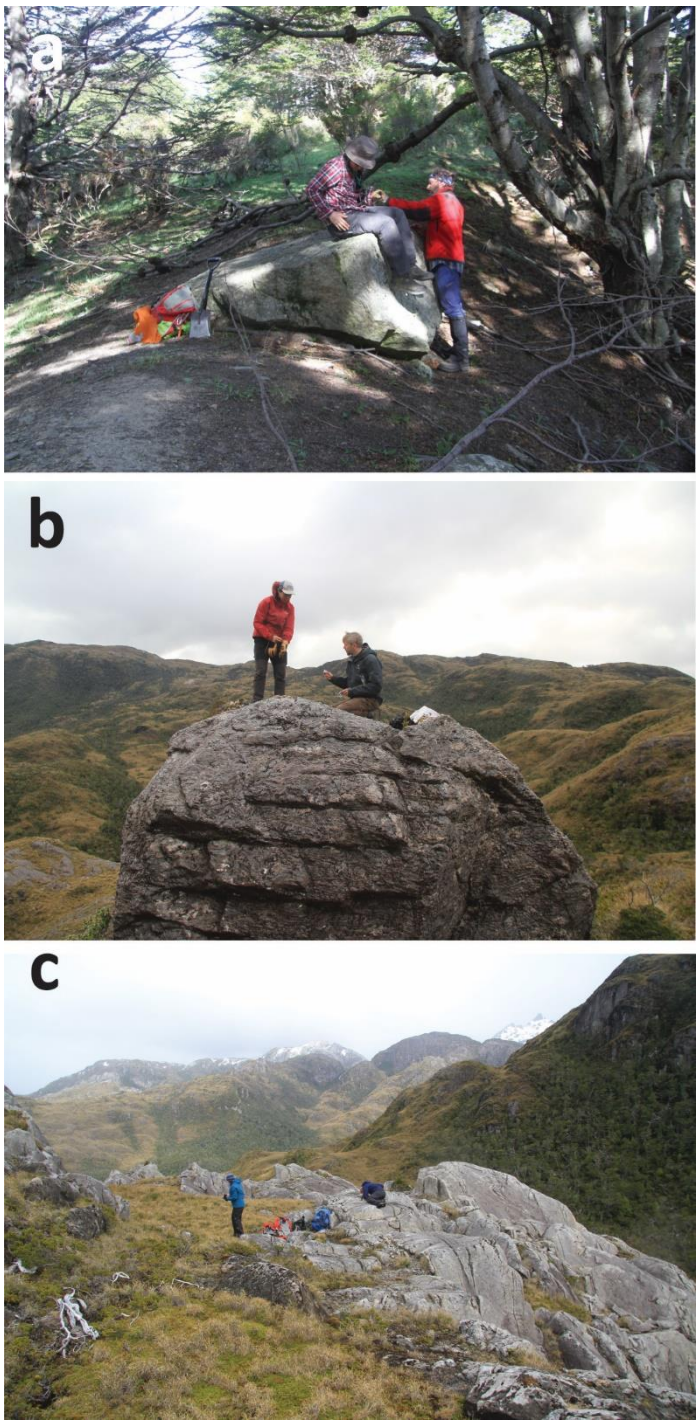

Figure 4. Examples of boulder and bedrock samples for cosmogenic surface exposure age dating: a) Río Condor, Canal Whiteside, moraine limit sample RC21-05, b) Estero Condor, Peninsula Cordova, erratic boulder sample EC22-02, c) Caleta Miller, Isla Cayetano, bedrock sample CM22-03.

surface erosion (e.g., striations and polish) were preferred. In selecting bedrock samples, we looked for evidence of glacial erosion (ice moulded bedrock), to increase the probability that inherited nuclides had been removed during the last glacial cycle. By collecting multiple samples of moraine boulders, erratic boulders, and glacially moulded bedrock from each site, we aim to identify

anomalous ages that could result from nuclide inheritance or post-depositional processes. Sample location was determined by use of a handheld GPS unit, and shielding from the surrounding topography was measured using a compass and clinometer and quantified using the code available in the online calculators formerly known as the CRONUS-Earth online calculators (Balco et al., 2008).

3.1.2 ^{10}Be Sample preparation

Physical and chemical preparation of all 47 samples were carried out at the University of Edinburgh's Cosmogenic Nuclide Laboratory following standard methods (Bierman et al., 2002; Kohl and Nishiizumi, 1992). Samples were crushed, milled, and sieved to isolate the 250-710 µm fraction. 1-2 etches in a 2:1 mixture of H_2SiF_6 and HCl were performed for four days on a shaker table to minimise non-quartz minerals. 3-4 further etches were performed in a 2% HF and 1% HNO_3 solution in a heated ultrasonic bath for 24 hours per etch to obtain pure quartz and remove meteoric ^{10}Be from the surface of quartz grains. Process blanks (n=6) and samples were spiked with 0.25 mg of ^{9}Be carrier (Scharlau Be carrier, 1000 mg/l, density 1.02 g/ml) and dissolved in concentrated (48%) HF. Once dried, the dissolved residue was fumed in $HClO_4$ to reduce the concentration of Boron in the samples and passed through an anion exchange chromatography column to remove Fe and other anions. The samples were precipitated to remove Ti and then passed through cation exchange columns to separate the Be and Al fractions. A final fume in $HClO_4$ was performed to keep Boron levels low and hydroxides of Be were precipitated and rinsed in 18MΩ water to purify the final AMS targets. The dried down hydroxide gels were oxidised at 900°C in a furnace. The resulting BeO was mixed with Nb at a 1:6 ratio and pressed into copper cathodes for AMS measurement at the Scottish Universities Environmental Research Centre (SUERC). ^{10}Be/^{9}Be measurements are normalised to the standards of Nishiizumi et al. (2007). Sample ^{10}Be/^{9}Be ratios presented in Table 1 include a mean blank ^{10}Be/^{9}Be (3.7×10^{-15}) correction that varied from 0.5-4.4% (normally 1-3%) of the sample ratio.

3.1.3 ^{10}Be exposure age calculations.

Cosmogenic ^{10}Be surface exposure ages were calculated using the online exposure age calculator formerly known as the CRONUS-Earth online calculator (version 3; Balco et al., 2008) using the LSDn scaling scheme (Lifton et al., 2014) and the local ^{10}Be production rate for southern Patagonia (Kaplan et al., 2011). Topographic shielding was never greater than 1.3% and thus has a negligible effect on exposure ages (Table 3). We do not include corrections for rock surface erosion, GIA uplift or shielding by snow, vegetation or soil cover and, therefore, we interpret our exposure ages as minimum ages. ^{10}Be exposure ages are reported as 'ka' (Table 1).

Table 1. Cosmogenic ^{10}Be surface exposure ages.

Sample ID	Latitude (dd)	Longitude (dd)	Alt. (m asl.)	Thickness (cm)	Topographic shielding correction	Quartz mass	^{10}Be concentration§ ± 1σ (atoms g^{-1}[SiO_2])	^{10}Be age (ka) ± 1σ (int)†	± 1σ (ext)†
Canal Whiteside									
PY21-01	-53.89713	-70.14562	31	3.5	0.99921	25.8161	80296±2345	**17.5±0.5**	1.5
PY21-02	*-53.89778*	*-70.14400*	*41*	*6.0*	*0.999937*	*27.5003*	*99512±6750*	***21.8±1.5***	*2.3*
PY21-03	*-53.89779*	*-70.14398*	*43*	*2.0*	*0.99986*	*38.667*	*201319±9646*	***42.4±2.1***	*4.1*
PY21-04	*-53.89733*	*-70.14449*	*38*	*2.5*	*0.999701*	*29.025*	*390563±7390*	***83.9±1.6***	*7.2*
PY21-05	*-53.89787*	*-70.14439*	*34*	*3.0*	*0.998922*	*27.6163*	*377384±5211*	***81.7±1.2***	*6.9*
PY21-06	-53.89639	-70.14801	24	2.5	0.999931	26.8359	84928±2793	**18.5±0.6**	1.6
PY21-07	-53.88363	-70.13663	32	2.5	0.999936	25.0702	80505±2546	**17.4±0.6**	1.5
PY21-08	*-53.88408*	*-70.1357*	*32*	*4.0*	*0.999726*	*36.8853*	*86999±2367*	***19.0±0.5***	*1.6*
PY21-09	*-53.88397*	*-70.13396*	*27*	*2.0*	*0.99939*	*41.0376*	*270708±7485*	***58.4±1.6***	*5.1*
PM21-01	*-53.93442*	*-70.1302*	*23*	*2.0*	*0.999783*	*26.9677*	*89641±6135*	***19.4±1.3***	*2.1*
PM21-02	*-53.93469*	*-70.12972*	*33*	*4.0*	*0.999779*	*25.7246*	*119975±4496*	***26.0±1.0***	*2.3*
RC21-01	-53.9431	-70.11724	20	5.0	0.999794	19.3563	69939±2695	**15.6±0.6**	1.4
RC21-02	-53.94551	-70.10284	39	3.5	0.999907	41.6585	79414±2088	**17.2±0.5**	1.5
RC21-03	-53.94505	-70.10444	35	1.0	0.999824	30.2738	71611±2237	**15.3±0.5**	1.3
RC21-04	-53.94459	-70.09521	54	2.5	0.999946	35.9813	81504±2222	**17.2±0.5**	1.5
RC21-05	*-53.94451*	*-70.09515*	*51*	*4.5*	*0.99985*	*38.7944*	*89021±3716*	***19.1±0.8***	*1.8*
Seno Otway - Canal Jeronimo (Estero Condor, Peninsula Cordova)									
EC22-01	-53.42026	-72.58438	83	1.5	0999051	30.7261	78095±2310	**16.1±0.5**	1.4
EC22-02	-53.42073	-72.5839	80	1.5	0.999051	28.7972	74673±2260	**15.5±0.5**	1.4
EC22-03*	-53.42072	-72.58388	78	1.0	0.99881	24.3394	73880±2346	**15.3±0.5**	1.3
EC22-04	-53.42014	-72.5843	79	2.5	0.999062	29.5217	77494±2492	**16.2±0.5**	1.4
Isla Santa Inés (Peninsula Ulloa)									
SI22-01	-53.70696	-72.41565	115	3.5	0.999025	31.3224	77569±1930	**15.7±0.4**	1.3
SI22-02*	-53.7069	-72.41552	111	3.0	0.999025	28.5679	79100±1900	**16.1±0.7**	1.5
SI22-03	-53.70714	-72.41594	117	2.0	0.999025	28.0978	82158±2505	**16.4±0.5**	1.4
SI22-04	-53.70106	-72.46625	79	2.0	0.982871	33.3564	83963±4030	**17.6±0.8**	1.7
SI22-05	-53.70109	-72.46632	78	2.0	0.98726	28.8028	76537±3508	**16.1±0.7**	1.5
SI22-06	-53.70115	-72.46643	77	1.5	0.988682	27.0077	70502±2219	**14.7±0.5**	1.3
SI22-07*	***-53.69987***	***-72.4663***	***69***	***1.0***	***0.989649***	***30.0685***	***97994±12630***	***20.0±2.6***	***3.1***
SI22-08	**-53.69978**	**-72.46606**	**69**	**7.5**	**0.989649**	**29.7432**	**71532±10440**	**15.8±2.3**	**2.6**
Isla Cayetano, Canal Barbara (Caleta Miller)									
CM22-01	-53.8737	-72.0899	122	1.0	0.99036	29.9524	77490±2533	**15.4±0.5**	1.4
CM22-03*	-53.87329	-72.07786	106	1.2	0.99619	28.6741	77441±2409	**15.5±0.5**	1.4
CM22-05	-53.86995	-72.08315	285	6.0	0.976937	32.0643	92713±2724	**16.6±0.5**	1.4
CM22-06*	-53.8699	-72.08498	275	1.0	0.999053	18.9996	96101±3323	**16.3±0.6**	1.5
CM22-07	-53.87252	-72.08447	229	1.0	0.998716	29.4349	88468±2099	**15.7±0.4**	1.3
CM22-08	-53.89074	-72.07803	164	5.0	0.998895	27.5127	75307±2441	**14.7±0.5**	1.3
CM22-09	-53.89067	-72.08241	224	2.0	0.99776	26.0755	93547±2898	**16.8±0.5**	1.5
CM22-10	-53.88929	-72.08543	229	1.0	0.997828	25.2309	91353±2296	**16.2±0.4**	1.4
Isla Clarence, Canal Acwalisnan (Seno Pedro and Punta Andrade – Seno Dyneley)									
SP22-01*	***-53.93661***	***-71.59311***	***40***	***2.0***	***0.999365***	***12.2821***	***128459±13145***	***27.2±2.8***	***3.6***

PA22-02*	-54.06801	-71.88973	135	2.0	0.99772	22.7906	81310±2607	**15.9±0.6**	1.4
PA22-04	-54.07006	-71.89252	98	2.0	0.997193	22.276	80600±2834	**16.3±0.6**	1.5
PA22-05	-54.07006	-71.89507	84	1.5	0.99441	26.9888	76975±2491	**15.8±0.5**	1.4
Canal Magdalena – Canal Cockburn (Pto Hope and Seno Chico)									
PH22-01	*-54.12252*	*-71.00008*	*161*	*2.5*	*0.998235*	*11.3672*	*100048±4302*	***19.0±0.8***	*1.8*
PH22-04*	-54.11963	-70.99637	260	1.0	0.998582	20.0586	88504±3144	**15.2±0.5**	1.4
PH22-05	-54.12063	-70.99799	244	1.5	0.998259	17.1817	83737±2699	**14.7±0.5**	1.3
SC22-01*	-54.43284	-71.14403	97	2.0	0.978132	25.2704	79343±2529	**16.3±0.5**	1.4
SC22-04	-54.43359	-71.14525	148	4.0	0.995867	28.6189	74496±2273	**14.5±0.4**	1.3
SC22-05	-54.43378	-71.14574	149	2.0	0.996807	26.477	87200±2538	**16.7±0.5**	1.4
SC22-06*	***-53.43378***	***-71.14574***	***149***	***3.5***	***0.996807***	***32.2259***	***94009±9975***	***18.2±1.9***	***2.4***

* All samples are from erratic boulders except for those with * which indicates a sample from glacially eroded bedrock.

Samples in bold have larger than normal uncertainties because of low beam currents (samples produced large precipitates from contaminants).

Anomalously older ^{10}Be ages are in italics and excluded from our chronology, likely due to nuclide inheritance from a previous exposure.

§ The concentrations are corrected for process blanks; uncertainties include propagated AMS sample/lab-blank uncertainty and a 2% ^{9}Be carrier mass uncertainty. ^{10}Be concentrations have been normalised to be consistent with 07KNSTD (Nishiizumi et al., 2007). AMS measurements made at the AMS facility at the Scottish Universities Environmental Research Centre, UK.

† Age calculations assume rock density 2.65 g cm^{-3}. No correction is made for rock surface erosion, GIA uplift or shielding by snow cover, vegetation or soil, and thus ages are minima. Exposure ages are calculated with the online calculator formerly known as the CRONUS-Earth online calculator (v.3.0; Balco et al., 2008) using the southern Patagonia local production rate (Kaplan et al., 2011), and the LSDn scaling scheme of Lifton et al. (2014). Internal uncertainties relate to analytical uncertainties; external uncertainties also include production rate and scaling uncertainties.

3.2 Luminescence dating

The timing of the lacustrine sediments associated with the 20-30 m asl. palaeoshoreline have been constrained by the Vn Reclus tephra layer (maximum age) and overlying peat layers (minimum age). To directly estimate the age of the lacustrine deposits we obtained nine luminescence ages using single grains of potassium-rich feldspar (K-Fs). All sample preparation and luminescence measurements were conducted at the Vienna Laboratory for Luminescence dating (VLL) at the University for Natural Resources and Life Sciences (BOKU), Institute for Applied Geology, Vienna. Samples were taken in light-tight cylinders and all sample preparation was conducted at the VLL under subdued red-light conditions. K-Fs grains in the grain size of 200-250 µm were prepared according to standard VLL procedures (Lüthgens et al., 2017; Rades et al., 2018). Equivalent dose values were determined on a RISØ TL-OSL DA 20 automated luminescence reader system (Bøtter-Jensen et al., 2000, 2003, 2010) using IR stimulation (830 nm IR laser) and detecting the luminescence signal by a photomultiplier through a LOT/Oriel D410/30 optical interference filter,

selecting the K-feldspar emission at 410 nm (Krbetschek et al., 1997). The applied IR50 SAR (single aliquot regenerative dose) protocol using a preheat temperature of 50°C for the dating of single grains of potassium-rich feldspar is described in detail in Garcia et al. (2019 and supplementary material provided therein). Based on the results from dose recovery experiments, the SAR rejection criteria were set to 20% for recycling ratio, 30% test dose error, signal >3σ above background. Most samples show clear indicators of incomplete bleaching: high overdispersion (calculated using the Central Age Model (CAM), Galbraith et al., 1999) and right-skewed dose distributions (all calculations using the R-Luminescence package of Kreutzer et al. ,2012). To account for the effects of incomplete bleaching, a bootstrapped three parameter Minimum Age Model (MAM, Galbraith et al., 1999; bootstrapping cf. Cunningham and Wallinga 2010) with a σ_b threshold of 3.5 ±0.5 was used for the calculation of an average equivalent dose for all samples except sample VLL-0573-L for which the CAM was used.

Table 2: Results from radionuclide analysis and luminescence dating of single grains of K-Fs for lacustrine sediment sections in the Strait of Magellan

Sample lab code[1]	**Sample field code**	**^{238}U (Bq/kg)[2]**	**^{232}Th (Bq/kg)[2]**	**^{40}K (Bq/kg)[2]**	**Overall doserate K-Fs (Gy/ka)[3]**	**K-Fs SG IR50 (n)[4]**	**K-Fs SG IR50 σ_b (%)[5]**	**K-Fs SG IR50 D_e (Gy)[6]**	**Fading corrected K-Fs SG IR50 age (ka)[7]**
VLL-0566-L	EC21 OSL1	24.6 ±2.7	30.5 ±1.3	488.4 ±36.1	3.2 ±0.2	73	57 ±6	22.3 ±0.8	**10 ±1**
VLL-0567-L	PA21 OSL1	17.4 ±1.9	21.0 ±0.9	390.7 ±28.9	2.5 ±0.2	46	61 ±9	19.5 ±1.1	**11 ±1**
VLL-0568-L	PA21 OSL2	15.4 ±1.9	17.9 ±0.8	395.7 ±29.3	2.5 ±0.2	59	44 ±7	23.5 ±1.0	**13 ±1**
VLL-0569-L	PCH21 OSL1	24.5 ±2.7	26.7 ±1.2	438.6 ±32.5	2.9 ±0.2	99	67 ±6	25.8 ±0.8	**13 ±1**
VLL-0570-L	PCH21 OSL2	19.3 ±2.1	21.7 ±1.5	408.7 ±30.2	2.6 ±0.2	104	66 ±6	29.1 ±1.0	**16 ±2**
VLL-0571-L	PM21 OSL1	23.5 ±2.6	31.5 ±1.4	538.3 ±39.8	2.8 ±0.2	78	48 ±6	23.5 ±0.9	**12 ±1**
VLL-0572-L	PM21 OSL2	22.1 ±2.7	27.9 ±1.5	408.7 ±30.2	2.7 ±0.2	73	34 ±7	20.0 ±0.7	**11 ±1**
VLL-0573-L	PM21 OSL3	21.1 ±2.3	27.4 ±1.5	368.8 ±27.7	2.6 ±0.2	99	41 ±5	16.4 ±1.0	**9 ±1**
VLL-0574-L	RC21 OSL1	19.4 ±2.1	23.4 ±1.2	448.5 ±33.2	2.8 ±0.2	46	50 ±8	33.3 ±1.3	**17 ±2**
VLL-0575-L	RC21 OSL2	20.2 ±2.2	22.8 ±1.2	468.5 ±34.7	2.9 ±0.2	43	42 ±9	23.2 ±1.4	**12 ±1**

[1] All measurements conducted at the Vienna Laboratory for Luminescence dating (VLL) at the University for Natural Resources and Life Sciences (BOKU), Vienna, Institute for Applied Geology.

[2] Determined using high-resolution, low-level gamma spectrometry. Measured at VKTA (Radiation Protection, Analytics & Disposal) Rossendorf, Dresden, Germany.

[3] Overall doserate: Cosmic doserate determined according to Prescott and Stephan (1982); Prescott and Hutton (1994), taking the geographical position of the sampling spot (longitude, latitude, and altitude), the depth below surface, as well as the average density of the sediment overburden into account. An uncertainty of 10% was assigned to the calculated cosmic doserate. External and internal doserate calculated using the conversion factors of Adamiec and Aitken (1998) and the β-attenuation factors of Mejdahl (1979), including an alpha attenuation factor of 0.08 ±0.01 and an internal K content of 12.5 ±0.5% (Huntley and Baril 1997) and an estimated average water content water content of 15 ±5 % (25 ±5 % for VLL-0571/0572/0573-L) throughout burial time.

[4] Equivalent dose values determined using an IR50 SAR protocol for the dating of single grains of potassium-rich feldspar (K-Fs) using a preheat temperature of 50°C as described in Garcia et al. (2019). Number of grains passing

all rejection criteria, which were set to 20% for recycling ratio, 30% test dose error, signal >3σ above background, based on the results from dose recovery experiments.

[5] Overdispersion (σ_b) calculated using the Central Age Model (CAM, Galbraith et al., 1999) using the R-Luminescence package (Kreutzer et al. 2012).

[6] Calculated using a bootstrapped three parameter Minimum Age Model (MAM, Galbraith et al., 1999, Cunningham and Wallinga 2010) with a σ_b threshold of 3.5 ±0.5 for all samples except sample VLL-0573-L for which the CAM was used.

[7] All ages calculated using the software ADELE (Kulig, 2005), fading correction according to Huntley and Lamothe (2001) using an average g-value of 3.73 ±0.24 as determined by fading tests conducted according to Auclair et al. (2003) for 12 aliquots for all samples except VLL-0566-L, VLL-0568-L, and VLL-0573-L.

For the determination of the external dose rate, radionuclide analyses were conducted at VKTA Rossendorf using high-resolution, low-level gamma spectrometry after storage of the samples for secondary secular Rn equilibrium. Activities for ^{238}U, ^{232}Th, and ^{40}K are provided in Table 2. All samples were found to be in secular equilibrium. The overall dose rate calculation included an alpha attenuation factor of 0.08 ±0.01, an internal K content of 12.5 ±0.5% (Huntley and Baril 1997) and an estimated average water content of 15 ±5 % (25 ±5 % for VLL-0571/0572/0573-L) throughout burial time. All ages were calculated using the software ADELE (Kulig 2005). Because K-Fs and an IR50 SAR protocol were used, all ages had to be corrected for anomalous fading (athermal signal loss over time, Wintle 1973). Fading experiments according to Auclair et al. (2003) for all samples except VLL-0566-L, VLL-0568-L, and VLL-0573-L yielded an average g-value of 3.73 ±0.24. This average g-value was then used for fading correction of all samples following the approach of Huntley and Lamothe (2001). All details on dose rate, age calculations, and luminescence ages (reported as 'ka') are provided in Table 2.

3.3 Radiocarbon dating

Six AMS radiocarbon dates provided by this study and 43 from the literature have been processed by a number of laboratories. All radiocarbon ages have been calibrated implementing the southern hemisphere curve SHCal20 (Hogg et al., 2020) and Calib ver.8.2 (Stuiver and Reimer, 1993). Radiocarbon ages are reported as 'cal ka BP' (BP = CE year 1950) (Table 3).

3.4 Tephrochronology

Nine tephra layers were identified in the field as discrete layers. Samples were cleaned of organic material and concentrated by acid digestion (Dugmore et al., 1992) and the mineral content of each sample was then assessed using light and polarising microscopy. Volcanic glass shards were identified based on morphology, vesicularity and isotropism under plane-polarised light. The major

Table 3: Radiocarbon ages calibrated using Calib ver. 8.2 (Stuiver and Reimer, 1993) and the SHcal20 curve (Hogg et al., 2020).

Site	^{14}C yr BP 1σ	Cal a BP range 2σ (median)	Laboratory code
Minimum ^{14}C ages for deglaciation of the Magellan cordilleran ice dome after Glacial Stage D			
Río Condor KH (53°56'S; 70°6'W)	11,858 ± 40	13,525 (13,682) 13,787	**SUERC-28038**
Río Caleta kame ter. KH (53°50'S; 70°9'W)	11,930 ± 45	13,599 (13,744) 14,001	**SUERC-28042**
JPC67 Almirantazgo M (54°19'S; 69°27'W)[a]	12,050 ± 60	13,781 (13,911) 14,053	**nr**
Puesto Miguelito MC (53°55'S; 70°7'W)	12,160 ± 40	13,811 (14,022) 14,106	**SUERC-28039**
Bahía Pía RB (54°59'S; 69°44'W)[b]	12,350 ± 120	14,026 (14,401) 14,959	**OS-64237**
Valle Holanda RB (54°56'S; 69°7'W)[b]	12,550 ±60	14,336 (14,751) 15,090	**OS-61638**
Punta Arenas, MC (53°09'S; 70°57'W)[c]	13 050 ± 95	15,271 (15,579) 15,860	**AA-30919**
Pampa Alegre, Sec (53°04'S; 70°51'W)[d]	13 155 ± 60	15,539 (15,733) 15,957	**SRR-6502**
Río Grande, KH (53°39'S; 70°30'W)[e]	13,223 ± 56	15,642 (15,828) 16,019	**SUERC-55287**
Est Guairabo, KH (53°19'S; 70°58'W)[c]	13,186 ± 78	15,535 (15,778) 16,034	**AA-42415**
Lago Ballena RB (53°38'S; 72°25'W)[f]	13,360 ± 40	15,840 (16,022) 16,196	**UBA-9751**
Est Esmeralda I, KH (53°37'S; 70°28'W)d	13,425 ± 310	15,253 (16,128) 17,032	**A-6807**
Laguna Arcilla RB (54°11'S; 71°33'W)[g]	13,530 ± 70	16,028 (16,266) 16,513	**nr**
Est California, KH (53°33'S; 69°26'W)[c]	13,614 ± 86	16,096 (16,394) 16,684	**AA-42414**
JPC77 Almirantazgo M (54°16'S; 69°47'W)[a]	13,650± 70	16,206 (16,443) 16,694	**nr**
Est Amarillo, KH (53°25'S; 70°59'W)[c]	13,849 ± 81	16,486 (16,766) 17,025	**AA-42416**
San Felipe, KH (53°36'S; 70°57'W)[c]	13,850 ± 90	16,461 (16,765) 17,035	**AA-35082**
Est Cameron II, KH (53°34'S; 69°29'W)[c]	13,980 ± 120	16,567 (16,930) 17,324	**AA-42413**
Punta Marinelli RB (54°20'S; 69°31'W)[b]	14,050 ± 70	16,821 (17,050) 17,340	**OS-61545**
Punta Burslem KH (54°54'S; 67°57'W)[h]	14,070 ± 70	16,880 (17,078) 17,351	**UCIAMS189863**
Punta Esperanza RB (54°18'S; 69°56'W)[i]	14,100 ± 40	17,003 (17,115) 17,328	**OS-119140**
Est Esmeralda II KH (53°35'S; 70°30'W)[c]	14,260 ± 350	16,362 (17,316) 18,216	**A-6793**
Puerto del Hambre RB (53°36'S; 70°56'W)[j]	14,470 ± 50	17,389 (17,603) 17,837	**CAMS-65903**
Lago Charquito KH (53°58'S; 70°3'"W)[k]	*16,130 ± 50*	*19,239 (19,441) 19,559*	***UCIAMS-171929***
Cerro Fox KH (53°52'S; 70°26'W)[l]	*17,154 ± 73*	*20,497 (20,676) 20,861*	***SUERC-76471***
Punta Yartou II KH (53°51'S; 70°8'W	*19,080 ±100*	*22,618 (22,976) 23,177*	***UCIAMS-189854***
Punta Yartou I KH (53°51'S;70°8'W)[m]	*21,880 ± 95*	*25,901 (26,098) 26,346*	***SUERC-28041***
Punta Yartou I KH (53°51'S;70°8'W)[m]	*22,690 ±75*	*26,481 (27,060) 27,230*	***SUERC-28515***
Maximum ^{14}C ages for formation of Late glacial lake (Lago Kawésqar) in the Estrecho de Magallanes			
Pampa Alegre, Sec (53°04'S; 70°51'W)			
Uppermost peat beneath terrace gravels[d]	12,720 ± 55	14,949 (15,123) 15,296	**SRR-6501**
Uppermost peat beneath terrace gravels[d]	12,820 ±100	14,972 (15,261) 15,589	**Beta-117943**
Peat immediately above Vn Reclus tephra[d]	12,070 ± 45	13,798 (13,916) 14,038	**SRR-4583**
Peat immediately above Vn Reclus tephra[n]	12,870 ± 200	14,436 (15,313) 15,954	**nr**
Peat immediately below Vn Reclus tephra[o]	12,310 ± 240	13,612 (14,393) 15,168	**A-6813**
Peat immediately above Vn Reclus tephra[n]	13,255 ± 250	15,140 (15,878) 16,621	**nr**
Peat immediately above Vn Reclus tephra[n]	13,580 ± 215	15,751 (16,355) 17,003	**nr**
Puente Charlie, Sec (53°26'S, 70°03'W)			
Intermediate peat layer 811 cm above base[d]	10,830 ± 50	12,695 (12,745) 12,834	**SRR-6499**
Intermediate peat layer 665 cm above base[d]	10,875 ± 45	12,730 (12,765) 12,890	**SRR-6287**
Intermediate peat layer 375 cm above base[d]	13,125 ± 55	15,489 (15,692) 15,902	**SRR-6498**
Intermediate peat layer 135 cm above base[d]	12,960 ± 55	15,258 (15,452) 15,643	**SRR-6497**

Intermediate peat layer 135 cm above base[d]	13,160 ± 45	15,575 (15,739) 15,921	**SRR-6288**
Peat layer 4 cm above Vn Reclus tephra[d]	13,205 ± 55	15,623 (15,803) 15,997	**SRR-6496**
Peat layer immediately below Vn Reclus tephra[o]	12,740 ± 120	14,513 (15,132) 15,574	**A-7569**
Vn Reclus tephra layer[p]	12,627 ± 48	14,578 (14,995) 15,181	**n/a**
Vn Reclus tephra layer[c]	12,638 ± 60	14,554 (15,004) 15,225	**n/a**
Minimum ^{14}C ages for drainage of the Late glacial lake (Lago Kawésqar) in the Estrecho de Magallanes			
Cabo Valentin II Sec. (53°34'S; 70°32'W)[c]	10,055 ± 65	11,264 (11,504) 11,759	**A-8164**
Río Caleta Sec. (53°49'S; 70°10'W)	10,110 ± 45	11,323 (11,621) 11,836	**UCIAMS-189853**
Cabo Valentin II Sec. (53°34'S; 70°32'W)[c]	10,314 ± 81	11,762 (12,048) 12,469	**AA-23077**
Río Caleta Sec. (53°49'S; 70°10'W)	10,430 ± 30	12,090 (12,284) 12,475	**Beta 414181**
Minimum ^{14}C age for Mid-Holocene marine incursion in the Estrecho de Magallanes			
Puerto del Hambre (53°36'S; 70°56'W)[h]	8265 ± 65	9017 (9202) 9415	**AA-35086**

Sample site codes: KH = kettle hole; M = marine; MC = meltwater channel; RB = rock basin; Sec. = section; nr = not reported. Anomalously older minimum ages for Glacial Stage D are in italics.

All ages from this study except: a Boyd et al. (2008); b Hall et al. (2013); c McCulloch et al. (2005b); d McCulloch et al. (2005a); e Mansilla (2015); f Fontana and Bennett (2012); g unpublished age from S. Björck; h McCulloch et al. (2020); i Hall et al. (2019); j McCulloch and Davies (2001); k Moreno et al. (2024); l Blaikie (2020); m Mansilla et al. (2016); n Stern (1992); o Clapperton et al. (1995); p Sagredo et al. (2011).

element geochemical composition of each tephra sample was determined by electron microprobe analysis using the SX100 Cameca Electron Microprobe at The University of Edinburgh (Hayward, 2012). A minimum of 10 glass shards were analysed to provide a representative geochemical signature (Hunt and Hill, 1993). Tephra identification was conducted through comparisons with geochemical data from previous studies (McCulloch and Bentley, 1998; McCulloch and Davies, 2001; Mansilla, et al., 2016, 2018; McCulloch et al., 2023).

3.5 Bathymetry

Hillshaded bed and lake/ocean bathymetric data are from ETOPO 2022 (NOAA, 2022) at 15 arc second resolution and referenced to the WGS84 ellipsoid. Figs. 3 and 13a-f were prepared in ArcGIS Pro 3.0. Map projection is WGS 1984 UTM Zone 19S.

3.6 Glacial isostatic adjustment modelling

As an independent check on the plausibility of the shallow continental shelf impounding a lake in the Estrecho de Magallanes during deglaciation, we used a GIA model. The aim was to see if the GIA model yielded relative sea-level changes consistent with the idea of the shelf producing a sill or dam above sea level during key periods of deglaciation. We emphasise that our intention was not to fully simulate the potential dam, but merely to test its plausibility with a reasonable set of ice loading and Earth model scenarios.

The GIA model used (Kendall et al., 2005; Milne and Mitrovica, 1998; Mitrovica and Milne, 2003) computes deformation of a spherically symmetric (i.e., 1D) Maxwell viscoelastic Earth in response to a global ice-loading model. Calculations were truncated at spherical harmonic degree 256, equivalent to a spatial resolution of ~78 km. We explored the results from two three-layer Earth models consisting of: an elastic lithosphere, upper mantle between the base of the lithosphere and 660 km depth, and lower mantle. The first model is consistent with seismic tomography mapping of the mantle viscosity in southern Patagonia (Mark et al., 2022) with a lithospheric thickness of 96 km, and upper mantle viscosity of 1×10^{20} Pa s. Whilst consistent with regional geophysical observations, this is a relatively 'weak' model in global terms and so we also explored an Earth model with a slightly 'stronger' structure with a lithospheric thickness of 120km and upper mantle viscosity of 1×10^{21} Pa s. The lower mantle viscosity is set to 1×10^{22} Pa s for both models.

For the ice loading we used the global ICE6G loading model (Peltier et al., 2015), but with the Patagonia component replaced by the output of a numerical ice model of the PIS (Fig. 5). The output comes from a full glacial cycle run of the Parallel Ice Sheet Model (PISM) applied to Patagonia (Lira, 2024). Climate is simulated by a positive degree-day model based on inputs derived from WorldClimate2 data (Fick and Hijmans, 2017) but scaled according to the results of a sensitivity analysis. In particular, the modern precipitation distribution is adapted to include a slight northwards expansion of the zone of maximum precipitation, acting as a proxy for a proposed northwards movement of the core of the Westerlies that deliver moisture to the ice sheet. The maximum precipitation is held at the same magnitude as modern. The spatial air temperature distribution is retained in terms of its modern pattern, but the time-evolving glacial-interglacial climate is forced by uniformly cooling the temperatures following the EPICA temperature curve for the last 120 ka (Jouzel et al., 2007), such that the air temperature reaches a maximum cooling of -8.5 °C compared to present at 24 ka. The model has been constrained against the PATICE synthesis of the past ice extent of the ice sheet at its maximum extent and at each of the PATICE deglacial time slices (Davies et al., 2020). The model fits the LGM PATICE extent well in all areas including the western Strait of Magellan but has slightly too much ice at the LGM in eastern Tierra del Fuego – this excess ice extent deglaciates rapidly after the LGM.

We generate relative sea level (RSL) curves for the sites Estrecho de Magallanes (Strait of Magellan west, SMW), Canal Barbara (CB), and Canal Cockburn (CC), located at the shallowest parts of the shelf at the mouths of the Estrecho de Magallanes and channels through the islands (Fig. 3, Table 4). In addition to generating RSL curves for the shelf we generated RSL curves for two regions where

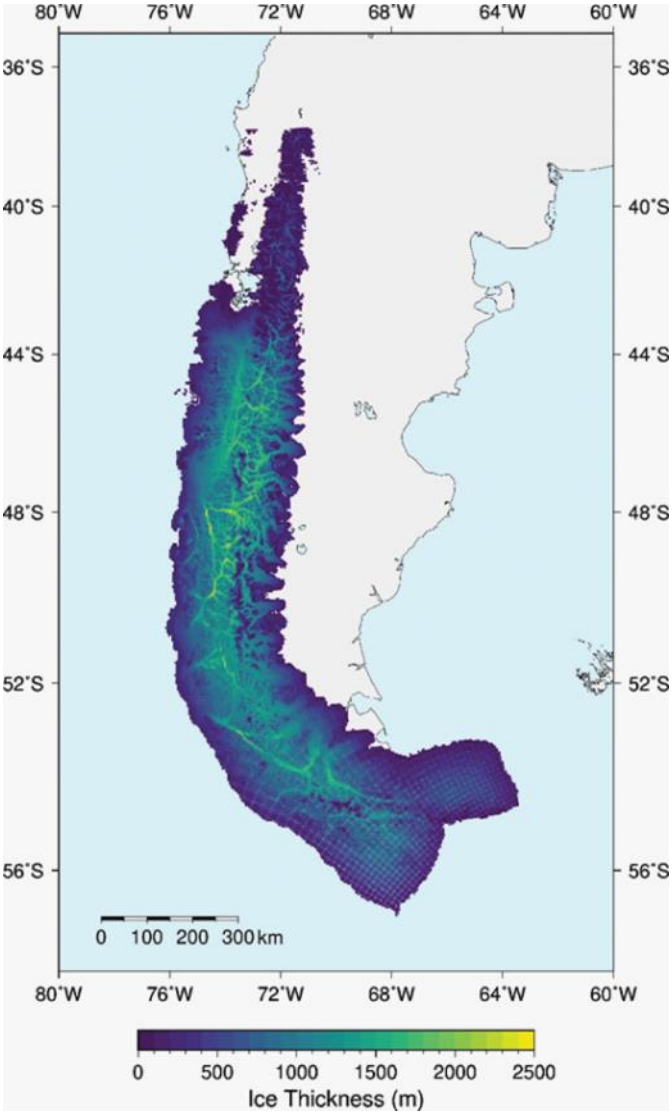

Fig. 5. Timeslice of the PIS output simulated with from the PISM model of Lira (2024). Model shows ice sheet thickness for 20 ka.

past RSL has been reconstructed using sediment core and raised beach data: namely the Argentinian shelf (AS-N and AS-S) (Guilderson et al., 2000) and the Estrecho de Magallanes, Bahía Gente Grande (BGG) and Puerto del Hambre (PdH) (Porter et al., 1984) (Fig. 3). Both published RSL curves compile data over a broad area so we generate representative RSL curves in two sites across the range of each of those compilations (Table 4).

4. Results and analysis

4.1 Lacustrine sediment sections

In addition to the raised palaeoshorelines that can be traced around the central section of the Estrecho de Magallanes and Bahía Inútil, three stratigraphic sections that contain lacustrine

sediments deposited above the Vn Reclus tephra layer have been described in detail by McCulloch et al. (2005b). The coastal site at Pampa Alegre (53°04'37"S, 70°51'58"W) is key. Here gully erosion has exposed a large sand and gravel unit, interpreted as a raised beach deposit. The sand and gravel unit overlies the Vn Reclus tephra, and its upper surface is a terrace which forms part of the ~20-30 m asl. raised shoreline (Figs. 6a and 6b) (Uribe, 1982; McCulloch et al., 2005b). At the base of the gully there is a small terrace ~4-6 m asl. comprised of fine marine sediments which have been incised by a small stream flowing down to the present sea. Two luminescence samples were taken from the lower (PA21-OSL1) and upper (PA21-OSL2) sandy layers of the beach deposit (Fig. 6b, Table 2). Eight ^{14}C ages have also been obtained from the organic rich sediments between the large sand and gravel unit and the underlying diamict (Fig. 6c, Table 3).

The coastal cliffs at Puente (Pte) Charlie (53°26'15"S, 70°04'07"W) contain ~25 m of lacustrine sediments overlying the Vn Reclus tephra (Fig. 7a). Deep gullies have been cut into the lower parts of a present-day alluvial fan forming steep cliff sections. Although the upper surface of the section is broadly consistent with the ~20-30 m asl. palaeoshoreline there are coarse alluvial sediments interbedded with the lacustrine sediments along with incision by stream activity and so there is no clear terrace surface. The floor of the gully has infilled to a small terrace surface at ~6 m asl. at the coast. Two luminescence samples (PCH-OSL1 and PCH-OSL2) were taken from the uppermost sand layers interbedded with finer lacustrine clay and silt layers to constrain the minimum age of the high lake stage (Figs. 7b and 7d, Table 2). Seven ^{14}C ages have also been obtained from thin (~1 cm) organic rich layers interbedded with the clay and silt layers (Fig. 7d, Table 3).

Two sites at Cabo Valentín, the northernmost point of the Isla Dawson peninsula, are short coastal sections close to present sea level (Fig. 8a). Cabo Valentín I contains a unit of ~1 m of laminated bluish-grey clays and silts above the Vn Reclus tephra layer deposited within peat (Fig. 8b). The upper surface of the section forms a terrace at ~8 m asl. and so there is no clear morphological link to the ~20-30 m palaeoshoreline. However, the fine sediments and the presence of drop-stones within the laminae suggest deep water conditions. At Cabo Valentín II, a ~1 m section has been exposed by coastal erosion that has cut into a diamict overlain by two layers of bluish-gray clays separated by the Vn Reclus tephra layer (Fig. 8c). Overlying the upper bluish-grey clay layer is a ~10 cm thick layer of well-humified peat which in turn is covered by a large unit of sands and gravels interpreted as a raised beach deposit. The upper surface of the palaeo-beach is ~8 m asl. and forms part of the mid-Holocene marine incursion palaeoshoreline. Two ^{14}C ages have been obtained from the peat layer immediately above the clay and silt laminae, which indicates drainage of the lake has been dated to c. 12.0 cal ka BP (McCulloch et al., 2005b) (Fig. 8c, Table 3).

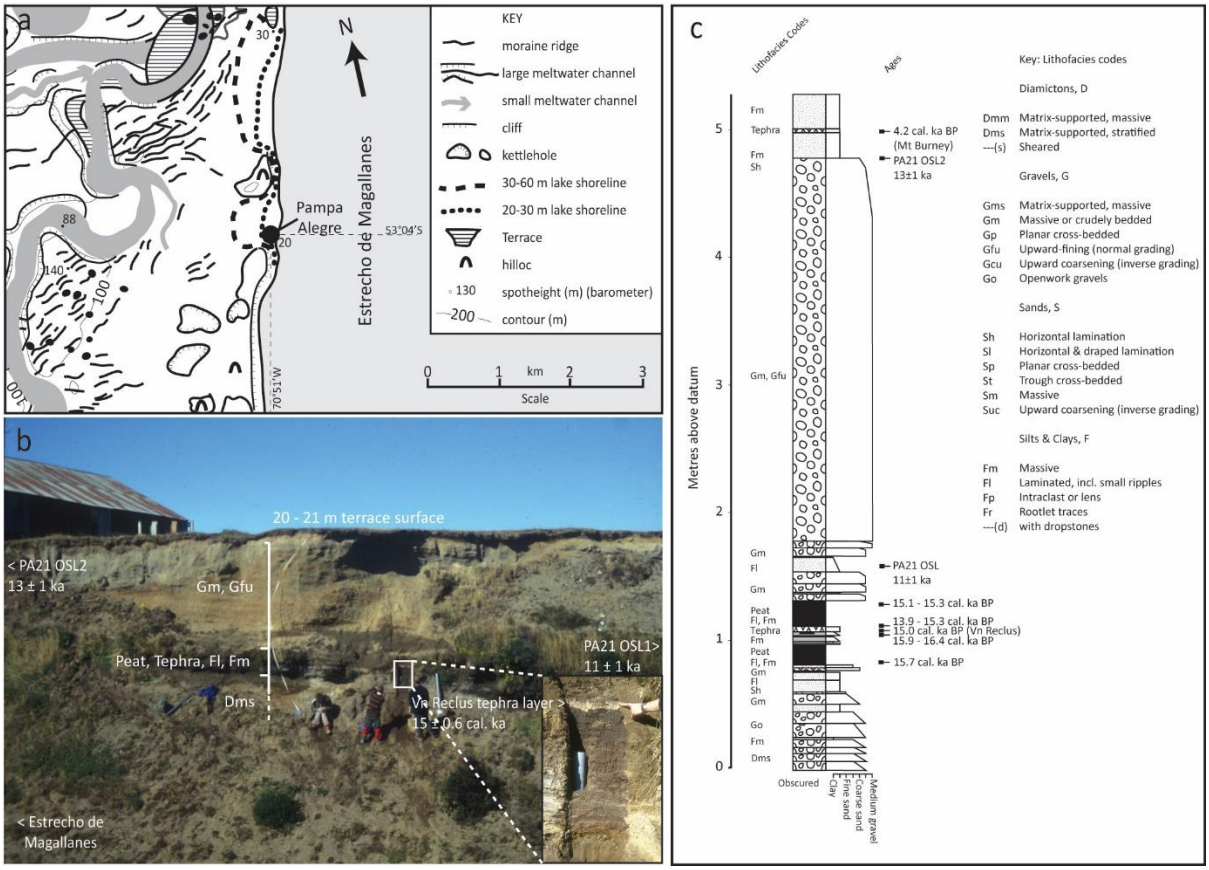

Figure 6. Key sampling locations for geochronology: a) extract of geomorphology map (from Bentley et al., 2005) indicating the location of the gully section at Pampa Alegre, north of Punta Arenas, and its association with the 20-30 m asl. palaeoshoreline; b) The gully section at Pampa Alegre and the location of OSL samples (inset image shows the Vn Reclus tephra layer beneath the unit of sands and gravels); c) Pampa Alegre stratigraphic section indicating the location of the ^{14}C ages (cal. ka BP) (Table 3). Lithofacies codes are from Eyles et al. (1983) and Benn and Evans (1998). These codes also apply to Fig. 7 and Fig. 8.

Field work as part of this study located two further stratigraphic sections: The first at Puesto Miguelito (53° 54' 31.9"S, 70° 8' 12.9”W) (Figs. 9a and 10a). A road-cut section ~15-17 m asl. reveals a peat layer overlying glacial diamict. Above the peat are layers of bluish-grey silt and fine-sand which is topped by colluvium and surface soils. At the contact between the peat and lacustrine sediments there is a fine intermittent white tephra layer and at the top of the lacustrine sediments, pockets of an olive-brown tephra layer were found. Three luminescence samples were taken from below the white tephra (PM-OSL1), the base (PM-OSL2) and middle (PM-OSL3) of the lacustrine sediments (Fig. 10a, Table 2).

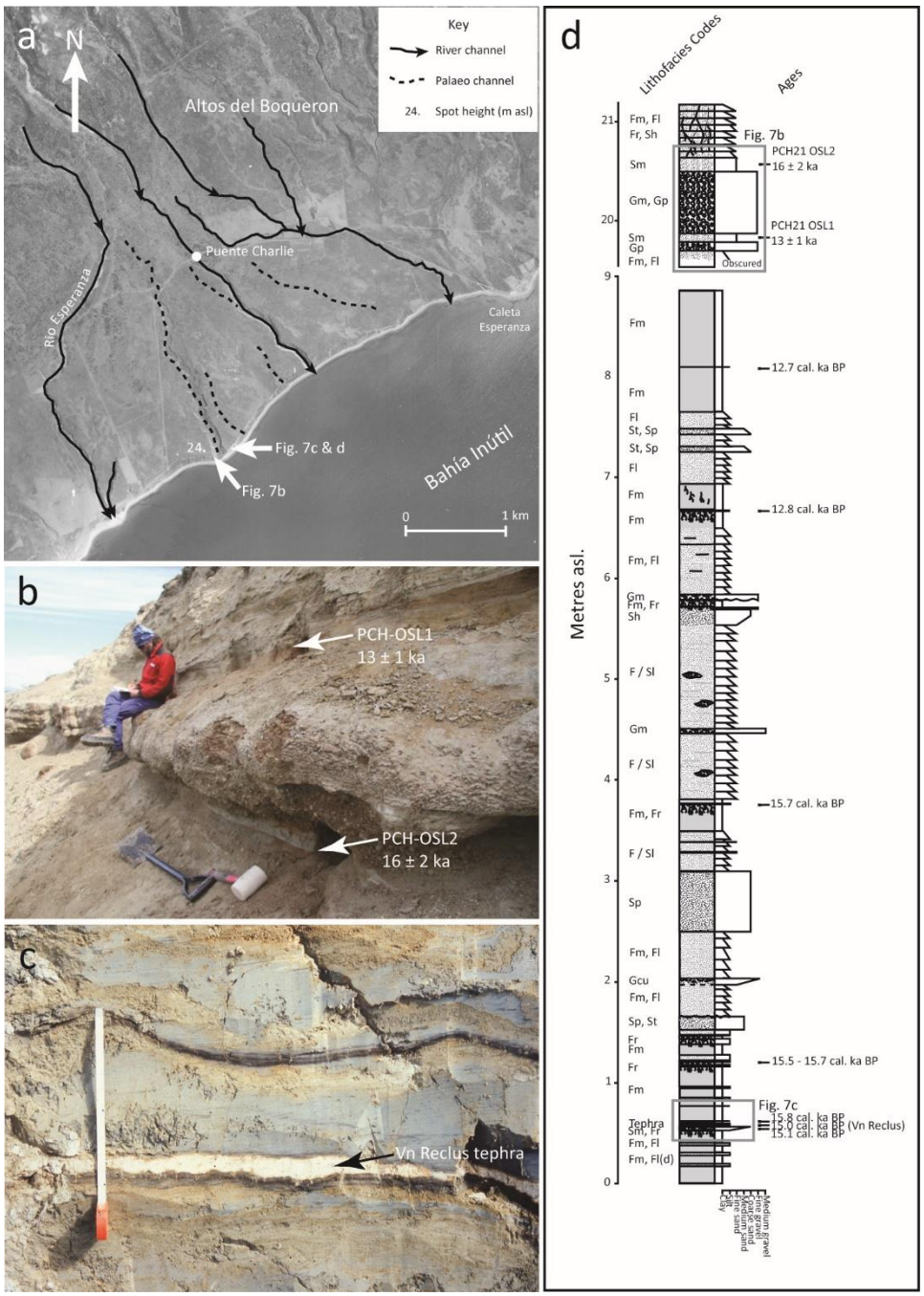

Figure 7. The cliff sections at Puente Charlie on the northern coast of Bahía Inútil: a) aerial photograph of the large alluvial fan at the foot of the glaciated slopes of the Altos del Boqueron and active and palaeo channels incised into the fan; b) The upper sediment layers at Puente Charlie cliff section and the location of OSL samples; c) the Vn Reclus tephra layer (~2-3 cm thick) within the lower clay and silt layers at Puente Charlie; d) Puente Charlie stratigraphic section indicating the location of the ^{14}C ages (cal. ka BP) (Table 3).

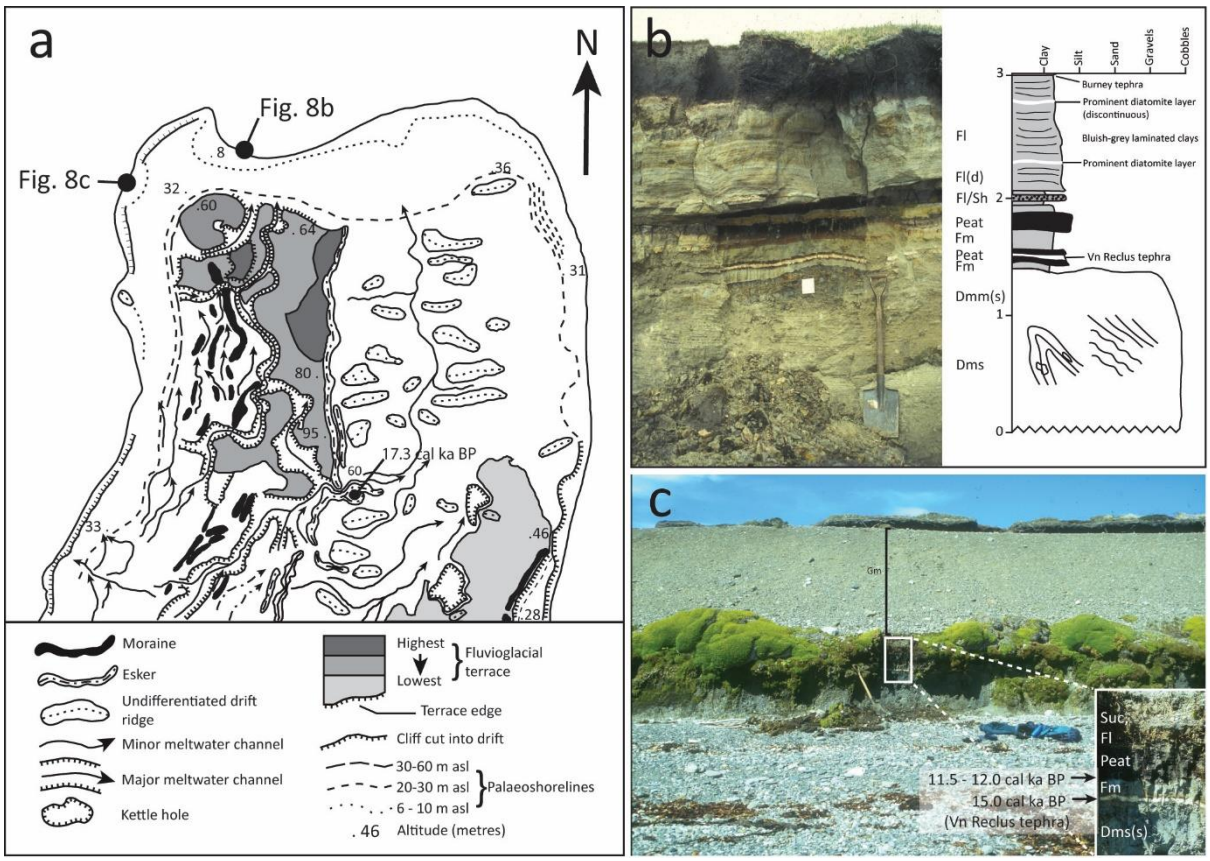

Figure 8. The low coastal sections at the north-western cape of the Isla Dawson peninsula: a) extract of geomorphology map (from Bentley et al., 2005) which indicates the spatial differentiation of the palaeoshorelines (30-60 m asl., 20-30 m asl. and 6-10 m asl.); b) Cabo Valentín I - laminated bluish-grey clays and silts overlying the Vn Reclus tephra and peat layers; c) Cabo Valentín II – massive bluish-grey clays overlying the Vn Reclus tephra. Two minimum 14C ages were obtained from the peat immediately overlying the upper bluish-grey clay layer (see inset figure).

The second site is a large cliff section at the southern margin of Río Caleta (53°54'31"S, 70°08'12"W) (Figs. 9a and 10b). The section comprises multiple layers of diamict overlain by a thin unit (~1-2 m) of lenses of fine gravels and sands fining upwards to fine sands and silts. This in turn is overlain by a unit (~5 m) comprised of bedded sands with ripple structures with a palaeosol close to the base of the unit. Two samples for luminescence dating were sampled from a sand layer above the uppermost diamict (RC-OSL1) and a bluish-grey sand layer from beneath the palaeosol (RC-OSL2) (Fig. 10b, Table 2). Two samples of the palaeosol were also sampled for ^{14}C dating (Fig. 10b, Table 3).

4.2 Glacial geomorphology of Canal Whiteside

Canal Whiteside is a north-south trending trough scoured by a large glacier that drained the north-eastern fjords of the Cordillera Darwin. The glaciers drained into Seno Almirantazgo and the flow was divided between a lobe that pushed eastward into Lago Fagnano and a lobe that pushed

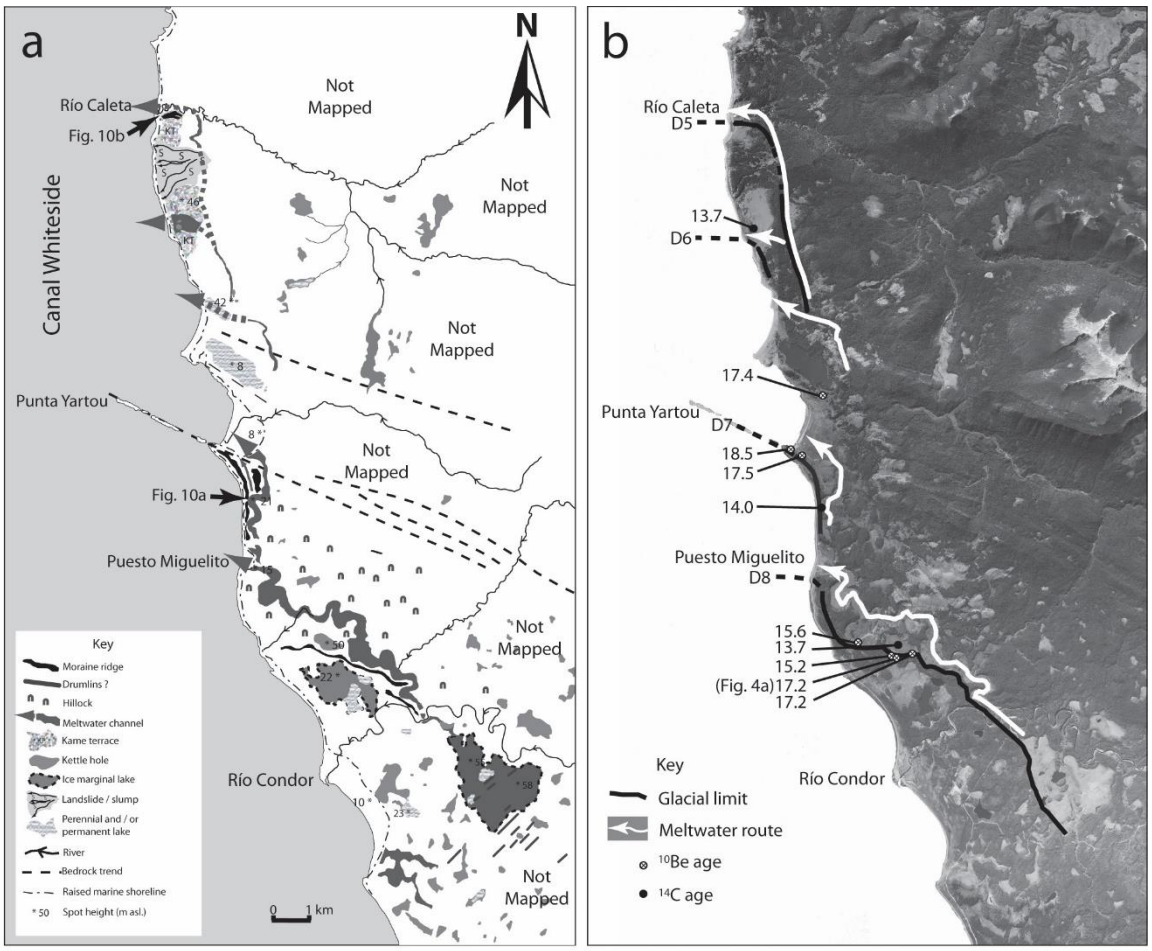

Figure 9. a) Geomorphology of the eastern shore of Canal Whiteside; b) Aerial photograph mosaic of the same area and inferred glacier limits during retreat after Glacial Stage D. Limits here labelled D5–D8 in continuation of mapped limits D1-D4 in Bahía Inútil (Bentley et al., 2005), although it is likely that there are further limits between D4 and D5.

northwards along Canal Whiteside, eventually merging with the Strait of Magellan glacier before being deflected into Bahía Inútil (Fig. 1b). McCulloch and Bentley (1998) identified moraine limits on the eastern and western sides of the northern peninsula of Isla Dawson suggesting advance / stand-still positions within Paso del Hambre and Canal Whiteside. Four ^{14}C minimum ages for ice retreat have been obtained from basal organic sediments sampled from kettle holes (Estancia (Est) Esmeralda I and II, Río Grande, Cerro Fox, Table 3). The three palaeoshorelines (30-60 m asl., 20-30 m asl., 6-10 m asl.), differentially uplifted to their higher altitudes in the south, are clearly demarcated on the northern peninsula of Isla Dawson (Fig. 8a). This study focused on the eastern shore of Canal Whiteside and involved glacial geomorphological mapping, sampling of erratic boulders for ^{10}Be dating, kettle holes for ^{14}C minimum ages, and the search for further sites with glacial lacustrine sediments overlying the Vn Reclus tephra layer.

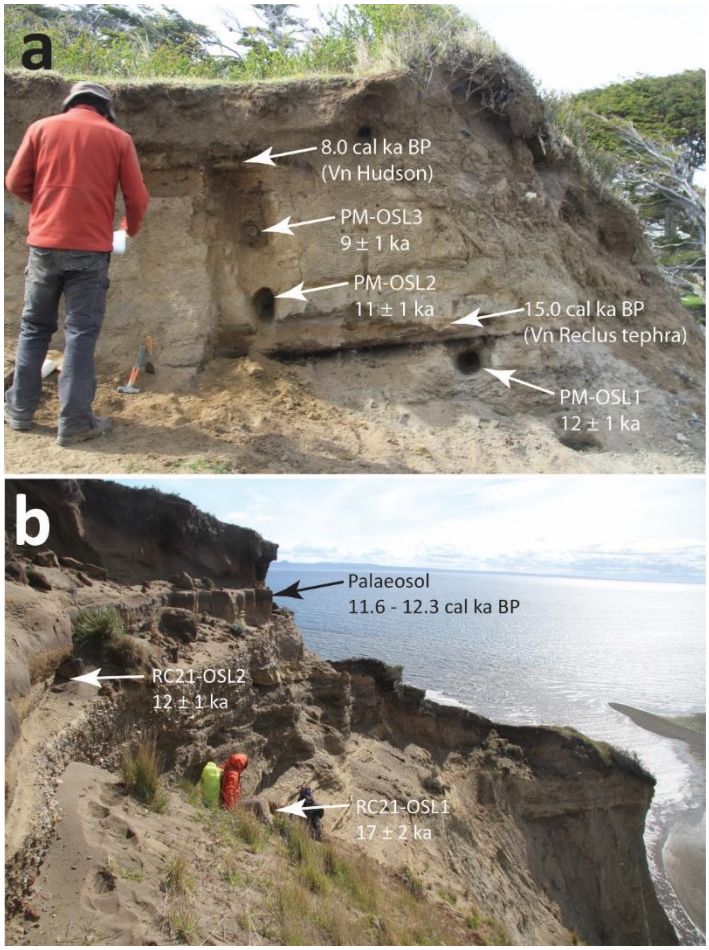

Figure 10. a) The sediment section at Puesto Miguelito, Canal Whitesite and laminated bluish-grey clays and silts overlying the Vn Reclus tephra layer and the location of three OSL sample points; b) The upper sediment layers at Río Caleta and the location of two OSL sample points.

A sequence of moraines and intervening meltwater channels run sub-parallel to the coast along the eastern side of Canal Whiteside (Fig. 9a). These record retreat of the former Whiteside glacier. The northern-most moraine is characterised by several low well-rounded ridges where a north-south trending meltwater channel heads offshore and, at the same point, the Río Caleta runs down to the present shoreline (Fig. 10b). Just south of this juncture is a kame terrace the surface of which lies at ~ 46 m asl. There are palaeochannels which indicate that the meltwater was able to cut a shorter route across the kame terrace to the shoreline (Fig. 9a). There are several large kettle holes in the surface of the terrace and at the head of the meltwater channel there are also two large kettle holes within the surrounding glacial drift. The surface of the drift is at ~ 50 m asl.

To the south of the kame terrace the topography is strongly bedrock controlled with two large bedrock lake basins within three bedrock spurs that extend out into Canal Whiteside. The southern bedrock ridge forms Pta Yartou. The southern (proximal) sides of the bedrock ridges are smeared with glacial drift and to the south of Pta Yartou the drift forms distinct ridges that run sub-parallel to the coastline. The most distinct ridge can be traced southward to just south of the Río Condor. A sinuous meltwater channel runs parallel to, and in places cuts into the glacial drift of this limit. The meltwater channel runs offshore at Puesto Miguelito at ~ 15 m asl (Fig. 9a). South of the Río Condor, a large flat area including lineated drift ridges following a north-east axis lies along the distal side of the moraine limit. Outside of this area the glacial geomorphology was obscured by the vegetation and lacked access.

To date the retreat of the former Whiteside glacier, sixteen erratic boulders with a granodiorite lithology, likely from the same source as the 'Darwin boulders' found in Bahía Inútil (McCulloch et al., 2005a; Kaplan et al., 2008; Evenson et al., 2009; Darvill et al., 2015), were sampled from the crests of the bedrock ridges and from the Río Condor moraine ridge for ^{10}Be surface exposure dating (Figs. 4a and 9a, Table 1). The kettle holes on the kame terrace and alongside the meltwater channel were also sampled for basal ^{14}C minimum ages (Fig. 9b, Table 3).

5. Discussion

5.1 Evidence for a Magellan pro-glacial lake

The evidence for the raised palaeoshorelines in the central section of the Estrecho de Magallanes and Bahía Inútil continues to be firm. The coastal gully section at Pampa Alegre contains near-shore (beach) sediments at ~17-20 m asl. These form part of a terrace that is an integral part of the ~20-30 m asl raised shoreline (Figs. 6a and 6b). The beach deposits overlie the Vn Reclus tephra layer (c. 15 cal ka BP) and ^{14}C ages from the organic sediments close above and below the tephra range from c. 15.1 to 15.7 cal ka BP (Fig. 6c, Table 3). Our luminescence ages sampled from the base and near the top of the beach deposits provide minimum ages of c. 11±1 and 13±1 ka respectively (Table 2). At the base of the gully is a small terrace infill formed during the mid-Holocene marine incursion indicating incision was completed sometime before c. 9.2 cal ka BP (McCulloch and Davies, 2001).

The stratigraphic evidence from Pte Charlie comprises ~25 m of bluish-grey clay / silt interbedded with coarse sediments, ranging from fine sand to cobbles, and occasional organic layers. The Vn Reclus tephra layer is visible in the basal sediments (~ 1 m asl) (Fig. 7c). The deep gullies perpendicular to the shoreline contain sediments from the mid-Holocene marine incursion thus indicating incision occurred sometime before c. 9.2 cal ka BP. The lacustrine sediments bracketed by

the Vn Reclus tephra and the ^{14}C ages suggest the lake was present between c. 15.0 and 12.7 cal ka BP. These ages are further supported by the luminescence ages from the uppermost fine sedimentary layers which provided ages for lake presence of 16±2 and 13±1 ka (Fig. 7b, Table 2).

The fine laminated bluish-grey clays and silts at Cabo Valentín I indicates the presence of a deep lake prior to and after the deposition of the Vn Reclus tephra (Fig. 8b) and the sub-aerial peat immediately above and below the tephra indicate the lake had lowered at that time. Two ^{14}C ages of c. 11.5 and 12.0 cal ka BP have been obtained from the peat layer immediately above the upper bluish-grey clay layer at Cabo Valentín II (Fig. 8c, Table 3). These ages are further constrained by the large sand and gravel unit that is a large, raised beach deposit. The upper surface of the raised beach is at ~8 m asl. and forms part of the mid-Holocene marine incursion palaeoshoreline.

The new stratigraphic section at Puesto Miguelito comprises bluish-grey clay / silt / fine sand sediments deposited above a well-humified peat layer. At the base of the silt / fine sand unit a silty creamy-white tephra layer has been geochemically linked to the Vn Reclus eruption. Luminescence samples from immediately below the Vn Reclus tephra and from the base and middle of the overlying silt / fine-sand unit have provided ages of 12±1, 11±1 and 9±1 ka respectively (Fig. 9a, Table 2). At the base of the colluvium overlying the silt / fine-sand unit, an intermittent olive-brown silty tephra layer is geochemically linked to the H1 eruption of Vn Hudson at c. 8.0 cal. ka BP.

The large river-cut section at Río Caleta comprises a sequence of diamict units interbedded with indurated outwash layers. The uppermost diamict grades upwards from coarse grit to bluish-grey silts and fine sand layers which in turn are overlain by more sand and grit layers. Overlying the bluish-grey sediments there is an extensive orange-drab sand unit which contains ripple bedding patterns, likely aeolian in origin. The palaeosol at the base of the aeolian unit has provided ^{14}C ages of 11.6 and 12.3 cal ka BP (Fig. 10b, Table 3). Luminescence ages from a bluish-grey fine-sand layer immediately above the diamict provided an age of c. 17±2 ka and a luminescence sample from the bluish-grey sand layer beneath the palaeosol provided an age of c. 12±1 ka (Table 2).

The kame terrace and altitudes of the meltwater channels running offshore between Río Caleta and Río Condor are included here as indicators of past water levels in the Strait. The kame terrace is ~ 46 m asl and a minimum age from a kettle hole in the surface of the terraces yielded an age of 13.7 cal ka BP. Minimum ages from the two kettle holes at the head of the Río Caleta meltwater channel provided ages of 22.9 (this study) and 26.0 – 27.0 cal ka BP (Mansilla et al., 2016). The meltwater channel eroded the wall of the northern kettle hole, and it is probable that the basal age from that kettle hole also indicates abandonment of the meltwater channel (Fig. 9b). Both kettle holes contain the Vn Reclus tephra. A basal sample from the Río Condor meltwater channel provided a minimum

age of 14.0 cal ka BP and a large peat basin (~50 m asl) on the distal side of the Río Condor moraine provided a minimum age of 13.7 cal ka BP.

5.2 Interpretation of the Magellan lacustrine evidence

The sequence of the palaeoshorelines indicate that the ~30-60 m asl high lake was formed during retreat of the Magellan cordilleran ice dome after Glacial Stage D. This is consistent with the luminescence date of c. 17±2 ka for the lacustrine sediments overlying the uppermost diamict at Río Caleta and with the minimum ages of c. 16.1 and 15.7 cal ka BP for the final drainage of the 30-60 m asl. Stage D lake (McCulloch et al., 2005a). At c. 15.0 cal ka BP the eruption plume of Vn Reclus spread over the region providing a key stratigraphic marker. The presence of peat beds close to present sea-level above and below the Vn Reclus tephra layer indicates that, following glacier retreat and lake drainage, the Estrecho de Magallanes was open to the Southern Ocean. Since global sea level was lower at this time, the central strait would have been a small marine embayment in the south and the northern area between the Segunda and Primera Angosturas would have been dry land. The Vn Reclus tephra was also found overlying bluish-grey clays and silts in the meltwater channel linking the Seno Otway proglacial lake to the Estrecho de Magallanes indicating abandonment sometime before c. 15 cal. ka BP (Mercer, 1976; McCulloch et al., 2005b).

Stratigraphic evidence strongly supports the interpretation that lacustrine sediments were deposited above the Vn Reclus tephra layer after c. 15.0 cal ka BP and that this event formed the ~20-30 m asl palaeoshoreline in the central Estrecho de Magallanes. The gully erosion of the lacustrine sediments down to below present sea-level and subsequent infill from the mid-Holocene marine incursion provides a broad minimum age constraint of c. 9.2 cal ka BP. However, ^{14}C dating of a peat layer overlying bluish-grey clays at Cabo Valentín II provides a closer minimum age for final lake drainage at c. 12.0 cal ka BP (McCulloch et al., 2005b). This is consistent with our luminescence minimum ages for the lacustrine units of c. 12±1 – 11±1 ka. The palaeosol at Río Caleta also provides a minimum age of c. 12.0 cal a BP for when the river graded to a higher water level and before incision and the formation of the mid-Holocene raised marine shoreline (~ 8 m asl.) at the base of the valley entrance. The presence of a large lake during the Late glacial is also supported by the presence of freshwater diatoms in the Strait followed by a transition to marine conditions as the Strait became open to the South Pacific Ocean between c. 10.5 and 8.5 cal. ka BP recorded in marine core MD07-3132 (G on Fig. 1) (Aracena et al., 2015).

5.3 Deglaciation of the Magellan cordilleran ice dome

Our evidence for the timing of glacial retreat is divided into two areas: firstly, the south-central section of the Estrecho de Magallanes (Canal Whiteside) and secondly, the fjords and channels of the Fuegian archipelago, including Canal Jeronimo.

The glacial geomorphological evidence from the eastern coast of Canal Whiteside, between Río Caleta in the north and Río Condor in the south, suggests at least four ice advances / stand-stills (D5-D8) (Fig. 9b). The most defined and continuous drift ridge extends southward from Puesto Miguelito to the Río Condor. South of the Río Condor the extensive flat peatland (~55 m asl.) covers a former ice marginal lake that drained through the sinuous meltwater channel parallel to the Río Condor moraine (D8 moraine in Fig. 9b). Our ^{10}Be surface exposure ages from Canal Whiteside present a wide range of ages from c. 83.9 to 15.2 ka, but the most consistent ages for the Río Condor moraine are between c. 15.3 and 17.5 ka. The moraine limits in Bahía Inútil are dated to c. 17.0 – 18.0 ka (McCulloch et al., 2005a; Kaplan et al., 2007) and deglaciation of the north-eastern fjords of the Cordillera Darwin has been constrained to c. 16.4 – 17.1. cal ka BP (Boyd et al., 2008; Hall et al., 2019). It is probable that the spread of older ^{10}Be ages between c. 83.9 and 19.0 cal ka BP is due to isotopic inheritance. The minimum AMS ages between c. 22.9 and 27.0 cal ka BP from plant fibres at the base of the two kettle holes near Pta Yartou are also inconsistent with the timing of the Stage D glacier retreat (Table 3). There is no stratigraphic evidence to suggest that the kettle holes are older landforms that have been overridden during Stage D. It is probable that there is a degree of freshwater error in the basal sediments of the kettle holes due to the accumulation of (carbonate-bearing) marl. However, 6000 to 9000 years of error would be unusual and difficult to account for within the plant fibres dated. Our other minimum ^{14}C ages from kettle holes and meltwater channels are between 13.6 and 14.0 cal ka BP (Table 3).

The glacial geomorphological and chronological evidence suggests that the Bahía Inútil – Canal Whiteside glacier retreated rapidly but in a stepped manner from its Glacial Stage D maximal position after c. 17.0 – 18.0 ka to the Pta Yartou area. It is probable that the topographic constriction between Isla Dawson and Pta Yartou led to a period of stabilisation (Fernández et al., 2017) as there are multiple stand-stills from Río Caleta and the kame terrace to the Río Condor limit and the formation of a large lateral glacial lake that drained northwards via the sinuous meltwater channel. The whaleback ridges are likely drumlins from a previous more extensive glacial advance that pushed further on land and became partially buried by the ice marginal lake sediments. The stepped retreat is consistent with the multiple moraine limits along the coasts of Bahía Inútil and Isla Dawson (Bentley et al., 2005; Fernández et al., 2017).

5.4 Deglaciation of the western Fuegian archipelago

Our ^{10}Be ages from the fjords and channels of the western Fuegian archipelago may be divided into three areas of interest: 1) Canal Jeronimo – Isla Santa Inés, 2) the fjords and interior of Isla Clarence, 3) Canal Magdalena – Canal Cockburn (Fig. 11). The Canal Jeronimo – Isla Santa Inés ages indicate the opening of Canal Jeronimo (location 1 on Fig. 1) at c. 15.3–16.2 ka and the retreat of the Isla Sta Inés ice field from across the western Estrecho de Magallanes by c. 15.7-16.4 ka. The channels (Canal Barbara and Canal Acwalisnan), fjords and interior of Isla Clarence were ice free by c. 15.4-16.6 ka and Canal Magdalena – Canal Cockburn was probably ice free sometime before 16.6 ka (Table 1). These ages consistently indicate that glacier retreat had reached close to present ice limits between c. 15.2 and 16.7 ka.

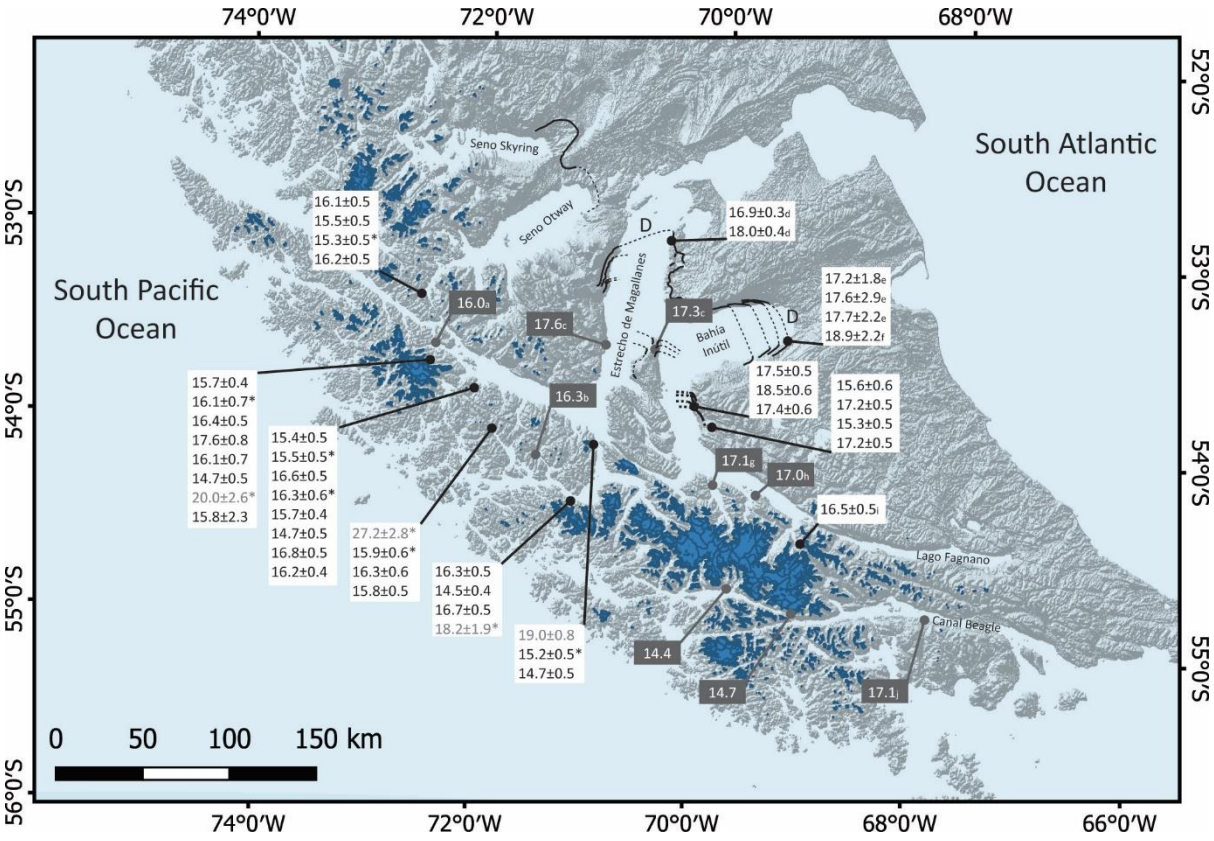

Figure 11: Minimum ages for glacier retreat from Stage D. The Stage D glacier limits (from Bentley et al., 2005, Lira et al., 2022). White boxes = ^{10}Be ages (samples in grey have larger than normal uncertainties because of low beam currents. Grey boxes = calibrated ^{14}C ages. All ages from this study except: a Fontana and Bennett (2012); b unpublished data S. Björck; c McCulloch and Davies (2001); d Peltier et al. (2021); e McCulloch et al. (2005b); f Kaplan et al. (2007); g Hall et al. (2019); h Hall et al. (2013); i Reynhout et al. (2022); j McCulloch et al. (2020).

5.5 The timing of deglaciation of the Estrecho de Magallanes

The cosmogenic ages for deglaciation of the western Fuegian archipelago are consistent with ^{14}C minimum ages from Isla Sta Inés of 16.0 cal ka BP (Fontana and Bennett, 2012) and Isla Capitán Aracena of 16.2 cal. ka BP (S. Björck, pers. Comm.). Our ^{10}Be ages from Canal Jeronimo (Estero

Condor), the southern entrance to Seno Otway, also suggest that it was ice free at c. 15.3-16.2 ka (Fig. 11). This is close to the timing of the abandonment of the Seno Otway meltwater channel at c. 15.0 cal ka BP, which indicates that the proglacial lakes in Seno Skyring and Seno Otway were able to drain into the Estrecho de Magallanes (McCulloch et al., 2005b).

Our minimum ages for deglaciation from Canal Whiteside (c. 15.3-17.5 ka) and the western Fuegian archipelago (c. 16.7-15.2 ka) are also contemporary with ages for glacier retreat into the north-eastern fjords of the Cordillera Darwin by c. 17.1 cal ka BP (Hall et al., 2019) and retreat from the eastern Canal Beagle sometime after c. 17.0 cal ka BP (McCulloch et al., 2020). Taken together the minimum ages for glacier retreat from this study and the literature indicate a comprehensive rapid and early retreat after the Stage D glacier advances into Seno Skyring, Seno Otway, the Estrecho de Magallanes, Bahía Inútil and the Canal Beagle. The ages from the Stage D maximal position and for retreat into the Fuegian archipelago fjords (a distance of ~140 km) are near synchronous, suggesting a threshold response of the glacial system to the more gradual southern hemisphere warming (Lüthi et al., 2008). We find no evidence for a significant glacier readvance into the Estrecho de Magallanes after Glacial Stage D.

6. Implications and probable solution for the Paradox

The results of our study and review of the extant evidence from the Magellan region presents two conclusions: 1) There was an extensive raised proglacial lake in the Estrecho de Magallanes between c. 15.0 and 12.0 cal. ka BP. 2) The Magellan cordilleran ice dome had retreated to the inner fjords of the Fuegian archipelago by c. 17.0-16.0 ka. The latter conclusion robustly indicates that there is no evidence for a Stage E glacier readvance capable of re-damming the Estrecho de Magallanes after the deposition of the Vn Reclus tephra layer. However, we still have the evidence for a ~20-30 m asl raised lake that requires an alternative geological/ geomorphological process to explain its formation and drainage. We suggest that the probable solution to this paradox lies in abandoning the inference that it was a 'proglacial' lake impounded by an ice dam and looking for an alternative geological / geomorphological process.

In exploring alternative mechanisms for impounding a lake we have considered mass movement processes and glacial isostatic adjustment. We note that there is no geomorphic (onshore or in bathymetry) evidence of large-scale (catastrophic) mass movement processes that would have been sufficient to dam the channels between the Estrecho de Magallanes and the South Pacific and Southern Oceans, the deposits of which might have been subsequently eroded to enable lake drainage. The remaining process of change of sufficient magnitude left to us is glacial isostatic adjustment (GIA). The early deglaciation of the Cordillera Darwin and the Fuegian archipelago would

have led to rapid rebound, primarily associated with the immediate elastic response of the Earth to ice loss. Estimates of GIA following deglaciation are few, but Troch et al. (2022) have estimated Late glacial and early Holocene uplift rates of ~13 mm a^{-1} for between the North and South Patagonian icefields (~48°S). The bathymetric data from the interior and around the Fuegian archipelago indicates that the main channels of the Estrecho de Magallanes (e.g. Paso del Hambre and Canal Magdalena) are deep but the southern continental shelf is shallow (~ -25 to -50 m asl), with the caveat that the resolution of the bathymetric data is limited (Fig. 3). We suggest that the early isostatic uplift of the Fuegian archipelago, including the continental margins, between c. 17.0 and 15.0 ka created a southern land barrier to drainage to the South Pacific and Southern Oceans. Continued uplift between c. 15.0 and 12.0 ka likely kept pace with any downcutting due to erosion at the overflow point (as yet unidentified). Such a gradual rising stage of the lake level is consistent with the interbedded lacustrine sediments and sub-aerial organic layers at Puente Charlie deposited as the delta / alluvial fan extended out into the rising Magellan lake.

6.1 GIA modelling of the southern Magellan region

The GIA model yields relative sea curves for the locations in Table 4 (see also Fig. 3), and we divide results into those from the weak and strong Earth models, respectively. The RSL curves for the Argentinian shelf match reasonably well the compilation from Guilderson et al. (2000) for both strong and weak Earth models (Fig. 12a and b). The Argentinian shelf RSL curves all show a major low stand at the global LGM followed by a steady rise in RSL reaching near-present by the Early Holocene (c. 8.0 ka). The Estrecho de Magallanes sites for a strong Earth show RSL was above present from c. 15.0 ka, reached a high stand in the mid-Holocene and has fallen thereafter (Fig 12a). This high stand is consistent in timing with the Porter et al. (1984) RSL curve but is much greater in magnitude. For the weak Earth model (Fig. 12b), the Argentinian shelf shows similar RSL behaviour (demonstrating the relatively small impact of ice loading on these sites) whilst the Estrecho de Magallanes sites show early high RSL, followed by a fall of RSL below present and then a Holocene high stand, with magnitude and timing similar to the Porter et al. (1984) curve.

For the western shelf sites, Estrecho de Magallanes west (SMW), Canal Barbara (CB), and Canal Cockburn (CC) (Fig. 3, Table 4), the sites are at ~30-50 m depth. The strong Earth model shows that RSL would have been relatively low and likely lower than some or all these depths (Fig. 12c). The implication is that sites at ~30 m present depth would not have been flooded until after c. 15.0 cal ka BP. They would have remained flooded thereafter.

In the weak model (Fig. 12d), RSL was initially relatively high and would have flooded all the shelf but RSL subsequently reached a minimum of ~ -30 m between c. 14.0 and 12.0 cal ka BP (Fig 12d) and any areas shallower than present 30m depth would have emerged as land.

6.2 GIA modelling discussion

The reasonable correspondence between the GIA model results and published RSL curves for the Argentinian shelf and the northern Estrecho de Magallanes show that the GIA model is yielding results that are consistent with geological data and give us more confidence in interpreting the

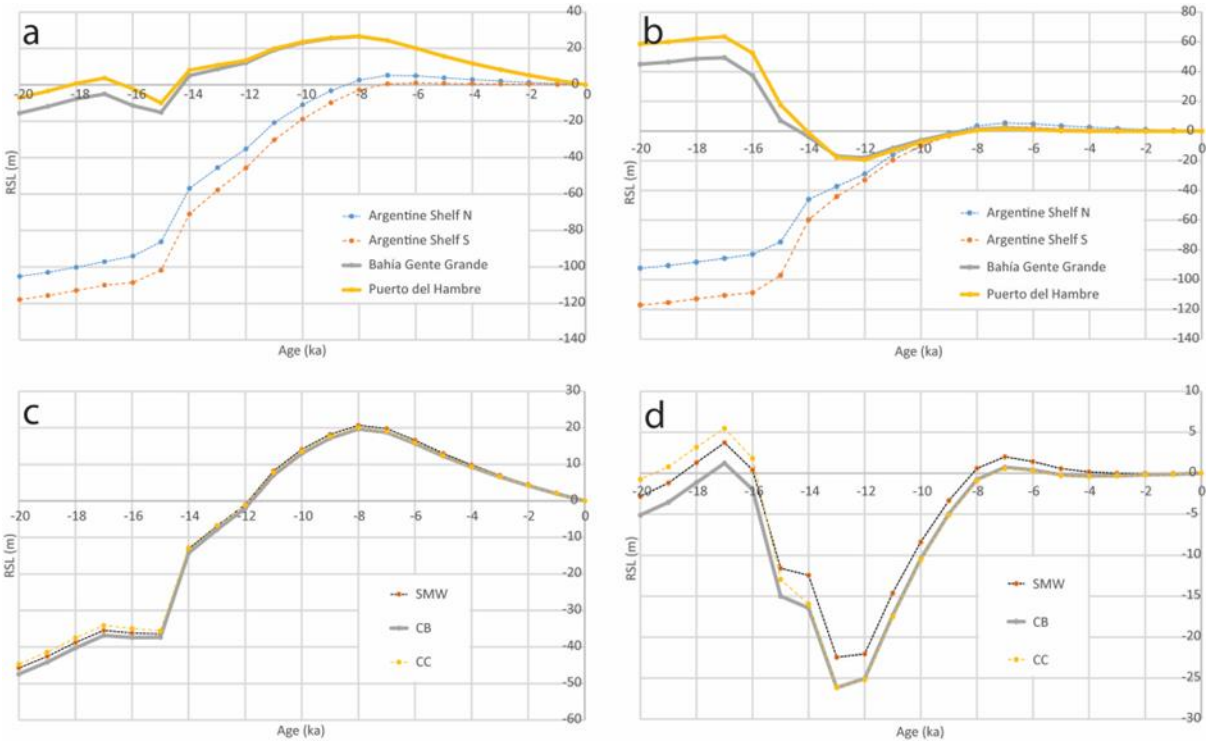

Figure 12. Relative sea level (RSL) predictions from GIA modelling. Atlantic shelf and central Strait of Magellan (a) Strong Earth model and (b) Weak Earth model. Pacific shelf (c) Strong Earth model and (d) Weak Earth model. Curves are labelled according to Table 4 and locations shown in Figure 3.

results from the western shelf where the RSL history is not geologically constrained. For these western shelf areas, the GIA model shows that both a weak and a strong Earth model produce RSL low stands sufficient to allow the shallowest parts of the western shelf to emerge as land during deglaciation. However, we do not claim the GIA modelling can demonstrate the precise magnitude or timing of such a low stand, as both are dependent on details of ice loading history and choice of Earth model parameters. Moreover, we note the clear limitations of using a global 1-D Earth model in the GIA modelling when a 3-D model would be necessary to fully simulate the GIA of this region, which has strong lateral viscosity contrasts (Mark et al., 2022). But our modelling work does show

that with (i) a geophysically-plausible Earth model and (ii) an independently-modelled ice sheet loading history consistent with geological constraints, then the shallowest parts of the western continental shelf may well have been dry land following deglaciation. Thus, shallow sills or dams, along the southern margins of the Fuegian archipelago sufficient to form a lake in the Estrecho de Magallanes and Bahía Inútil (and which also extended through Canal Jeronimo to Seno Otway and Seno Skyring) appear to be plausible.

6.3 Final lake drainage of the Estrecho de Magallanes

We suggest that GIA following rapid glacial unloading of the Fuegian archipelago and Cordillera Darwin probably dammed the southern margin of the Estrecho de Magallanes and allowed the formation of the 20-30 m asl. lake after c. 15.0 cal ka BP. However, postglacial isostatic uplift is a continuing process, as evidenced by the mid-Holocene marine raised shoreline. The field evidence indicates final drainage of the 20-30 m asl. lake at c. 12.0 cal ka BP. Lake lowering due to down cutting of the lake spillway, either to the north through the eastern Estrecho de Magallanes (through the Primera and Segunda Angosturas) or to the south through Canal Magdalena, appears unlikely because the rate of erosion of bedrock would have had to have been faster than the rate of uplift of the sills and RSL rise. In both our weak and strong Earth model GIA simulations RSL would have been rising fairly rapidly by 12 ka (Fig. 12).

Here we suggest that the removal of the southern land barrier to lake drainage may have been abrupt, and caused by a downward movement along the Magellan-Fagnano fault system and associated shear-strain zone. Bentley and McCulloch (2005) have already suggested that during the Early Holocene, localised down-faulting of a graben at Puerto del Hambre lowered the peat bog at least ~30 m, to below the ~20-30 m asl shoreline: this is indicated because the peat stratigraphy contains no lacustrine deposits between the Vn Reclus tephra layer and the Holocene but does contain evidence of the Early Holocene marine incursion. Thus, it had to have moved from above the former lake to (close to) its present position between these two events, requiring a rapid, probably tectonic explanation (Bentley and McCulloch, 2005). However, here we argue that the extent of the down-faulting was wider than previously suggested. The kame terrace at Pta Yartou presently lies at ~46 m asl but was formed during a still-stand during glacier retreat after the Stage D advance at c. 17 cal ka BP. The location of the kame terrace in relation to the Stage D palaeoshorelines indicates that it should be ~ 75 m asl and so points to a downward displacement of ~30 m (Fig. 2). To the south of the Pta Yartou boundary, the order of downwards movement was likely greater as evidenced by the sinuous meltwater channel at Puesto Miguelito. The latter is a Stage D feature but enters Canal Whiteside at ~ 15-17 m asl. indicating a drop of ~60 m.

South of the Pto del Hambre – Pta Yartou shear-strain zone the rising trends of the 30-60 m asl. (Stage D) and 20-30 m asl. Late glacial palaeoshorelines, due to differential isostatic uplift, are truncated and lower palaeoshorelines dip southwards and eventually disappear below present sea-level (Fig. 2). However, the mid-Holocene marine incursion raised shoreline can be traced further south. We suggest that downward vertical movement along the MFFS has submerged the southern higher palaeoshorelines. The bathymetry map of the Fuegian archipelago hints at shallow palaeochannels south of Canal Magdalena which may have been scoured as the lake drained to the Southern Ocean, but in the absence of higher resolution bathymetry this is speculative. Downfaulting along the MFFS may have continued into the Early Holocene after the lake drained but stabilised before the mid-Holocene marine incursion.

It is likely that the neotectonic downfaulting along the MFFS was abrupt, leading to rapid drainage of the Magellan lake at c. 12.0 cal ka BP. Glacially-induced faulting associated with GIA has been identified within stable intracratonic areas of North America and Europe, particularly Scandinavia. Large magnitude seismic events tend to occur within ~ 2 ka of deglaciation. 'Single event seismic displacements' of up to 18.5 m have been observed (Steffen et al., 2014). Therefore, larger, and multiple events are likely along an active plate boundary.

Figure 13 provides a summary schematic of the sequence of events in the Estrecho de Magallanes. Starting from the advance of the major glacier lobes to the large moraine limits that formed the Segunda Angostura (Glacial Stages B and C, Bentley et al., 2005) (Fig. 13a) and followed by the relatively smaller glacier advance (Glacial Stage D) sometime before c. 18.0 ka including the formation of the proglacial lakes at the heads of Magellan and Bahía Inútil glacier lobes (Fig. 13b). During the rapid retreat of the Magellan glaciers c. 18.0-17.0 ka the Estrecho de Magallanes and Bahía Inútil proglacial lakes unified thus forming the full extent of the 30-60 m asl. (Stage D) proglacial lake (Fig. 13c). Sometime between c. 16.0 and 15.0 ka the southern ice dam broke and the Glacial Stage D proglacial lake likely catastrophically drained to the Southern Ocean probably through Canal Magdalena or the western approach of the Estrecho de Magallanes (Fig. 13d). During this time the Estrecho de Magallanes was a marine embayment, open to the South Pacific and Southern Oceans but closed to the South Atlantic Ocean. At c. 15.0 cal. ka BP the eruption of Vn Reclus deposited the key chronostratigraphic tephra layer over the south-west of the region. Between c. 15.0 and 12.0 ka there is strong sedimentological and chronological evidence for the reforming of a large lake in the Estrecho de Magallanes and Bahía Inútil. Here we argue that early and rapid uplift after glacier retreat led to the formation of a topographic barrier along the present

shallow marine shelf of the Fuegian archipelago (Fig. 13e). It is likely that this lake also extended via Canal Jeronimo into Seno Otway and Seno Skyring.

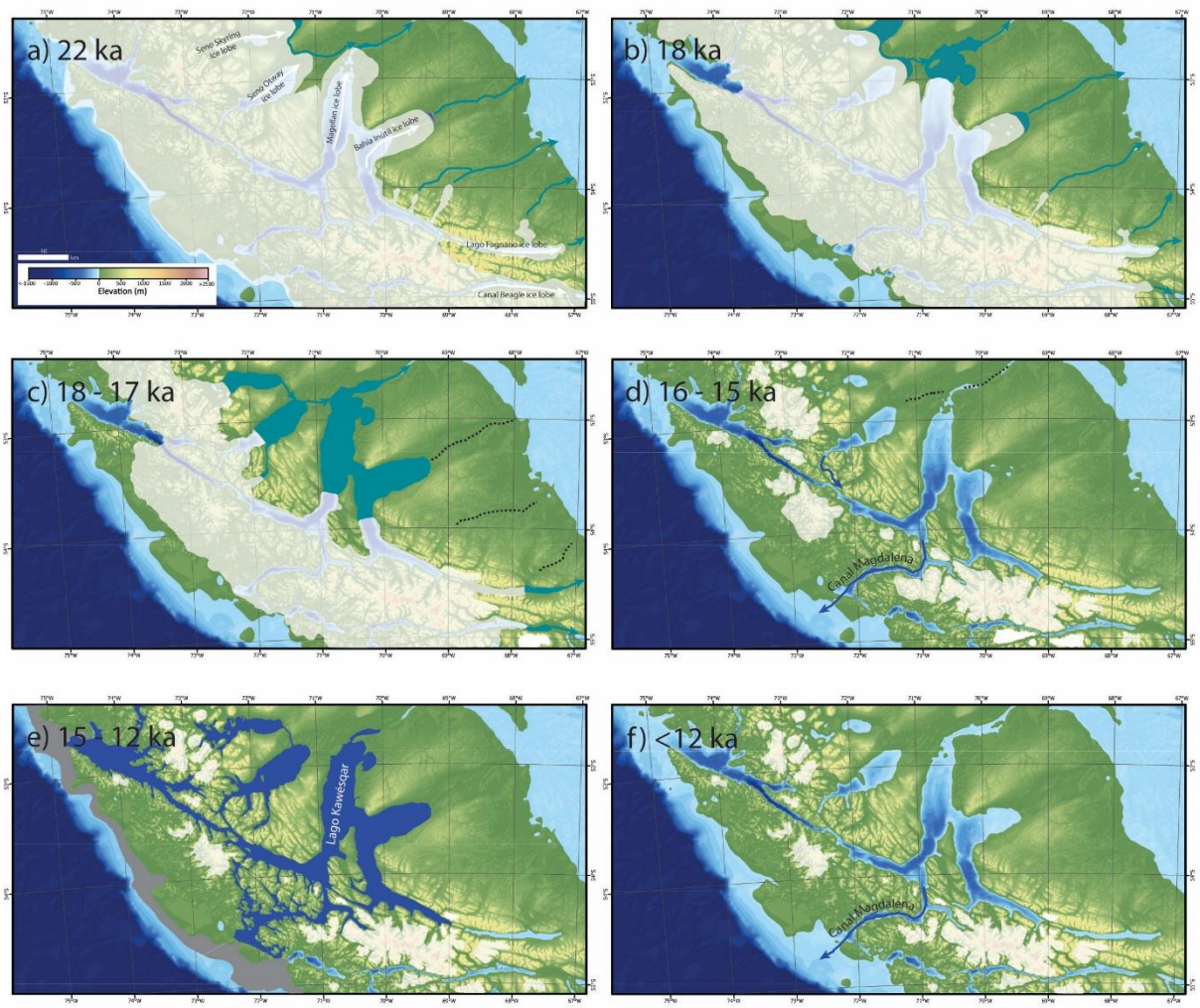

Figure 13. A schematic reconstruction of the sequence of events in the Estrecho de Magallanes during the LGIT: a) c. 22.0 ka, an advance of the Magellan cordilleran ice dome to the Segunda Angustura and meltwater drainage routes to the South Atlantic (Glacial Stage C, Clapperton et al., 1995; McCulloch et al., 2005b); b) c. 18.0 ka, a readvance or stand still of the Magellan cordilleran ice dome (Glacial Stage D). At this time relatively small proglacial lakes formed at each glacier lobe which continued to drain via large meltwater channels to the South Atlantic; c) c. 18.0-17.0 ka, a mid-point of recession of the Magellan cordilleran ice dome and expansion of the proglacial lakes which continued to be held in place for as long as the cordilleran ice dome continued to block the channels, i.e. potential meltwater drainage routes, through the Fuegian archipelago to the south and west; d) c. 16.0-15.0 ka, widespread retreat of the Magellan cordilleran ice dome leading to the eventual collapse of the ice dam along the Fuegian archipelago and rapid drainage of the Stage D proglacial lake and abandonment of meltwater drainage routes. This was closely followed by the eruption of Vn Reclus and the deposition of the key chronostratigraphic tephra layer; e) c. 15.0-12.0 ka, following the early and rapid recession of the Magellan cordilleran ice dome, isostatic uplift of the Fuegian archipelago and Cordillera Darwin raised the present shallow shelf (grey shaded area) that formed a topographic barrier to drainage of the central Estrecho de Magallanes and the formation of a large extended lake, including Seno Otway and Seno Skyring, here named ‘Lago Kawésqar’ (D. f) c. 12.0 ka, neotectonic downfaulting along the MFFS led to a drop of the Fuegian archipelago resulting in the final drainage of Lago Kawésqar and the flow of marine waters into the Estrecho de Magallanes from the South Pacific Ocean.

The palaeoshoreline and sedimentary evidence has previously been used to infer a readvance of the Magellan cordilleran ice dome, termed Glacial Stage E (McCulloch and Bentley, 1998, McCulloch et al., 2005b). However, our paradigm shift argues for a non-climatic mechanism for the formation of the large lake in the Estrecho de Magallanes and wider area. Therefore, referring to the lake as Glacial Stage E or coeval with the ACR is inappropriate. The palaeolake occupied more than the Estrecho de Magallanes thus the 'Palaeolake Magellan-Bahía Inútil' (Davies et al., 2020) is also not ideal. Here, we suggest the name 'Lago Kawésqar' after the canoe-people that occupied the Fuegian Archipelago. Final drainage of Lago Kawésqar at c. 12.0 ka was likely rapid due to neotectonic downfaulting along the MFFS and the Estrecho de Magallanes and interior marine embayments were open to marine waters (Fig. 13f). The connection between the South Pacific and South Atlantic Oceans through the Estrecho de Magallanes occurred later sometime prior to 9.2 cal. ka BP (McCulloch and Davies, 2001).

7. Conclusion

We have revisited published evidence and presented new sedimentary and dating evidence that confirms the presence of a large Late glacial lake, 'Lago Kawésqar', in the Estrecho de Magallanes between c. 15.0 and 12.0 cal ka BP. We have also presented new dating evidence for the widespread and rapid retreat of the Magellan cordilleran ice dome to near present ice margins by c. 16.5 ka. The evidence for the extent and timing of glacial retreat strongly indicates the lack of a glacier readvance capable of damming the southern drainage of the Estrecho de Magallanes. This and the evidence for a large Late glacial lake has presented a paradox. Here we resolve that paradox by suggesting that GIA following deglaciation after c. 18.0 ka led to early and rapid uplift of the southern margins of the Fuegian archipelago which in turn led to a land barrier and the formation of Lago Kawésqar in the Estrecho de Magallanes. With (i) a geophysically plausible Earth model and (ii) an independently modelled ice sheet loading history consistent with geological constraints, the GIA modelling shows that the shallowest parts of the western continental shelf may well have been dry land at certain intervals following deglaciation. Thus, we have shown it is plausible that they created a barrier permitting the build-up of a large lake in the Estrecho de Magallanes and neighbouring Seno Otway and Seno Skyring. Final drainage of Lago Kawésqar at c. 12.0 cal ka BP was probably caused by one or more seismic displacement events along the MFFS. Increased seismicity was likely enhanced by higher stresses during rebound following deglaciation. Our conclusions provide a resolution to the problem presented by the evidence for early deglaciation and yet the presence of a Late glacial lake in the Estrecho de Magallanes. Importantly, it forces a re-evaluation of any climatic inferences drawn from the lake evidence and the lack of a substantial glacier advance during the ACR.

Acknowledgements

This research was supported by the Chilean National Agency for Research and Development: FONDECYT 1200727 Agencia Nacional de Investigación y Desarrollo de Chile (ANID). M-PL was supported by a PhD studentship from ANID PFCHA/Doctorado Becas Chile/2018—72190469 and CH was supported by an E4 DTP NERC Studentship (NE/S007407/1). We are grateful to Dr. Chris Hayward for assistance in our use of the Cameca SX100 Electron Microprobe in the School of GeoSciences, The University of Edinburgh, and Prof. Gordon Cook at the SUERC Radiocarbon Laboratory, East Kilbride, for advice and support with radiocarbon dating. Fieldwork in the Parque Nacional Alberto de Agostini was permitted by the Corporación Nacional Forestal, Dirección Regional Magallanes y Antartica Chilena Doc. 247/2020 and the Armada de Chile provided logistical support and access to Isla Dawson. We also thank Rodrigo Genkowski and Tatiana López for supporting our work around Puerto Yartou. We thank the crew of the MV Chonos, Mary McCulloch, Fraser MacDonald, and Euan Robertson for their assistance with field sampling. We are grateful to David Sugden for comments on an earlier version of the manuscript.

References

Adamiec, G., Aitken, M., 1998. Dose-rate conversion factors: update. Ancient TL, 16: 37-50.

Aracena, C., Kilian, R., Lange, C.B., Bertrand, S., Lamy, F., Arz, H.W., De Pol-Holz, R., Baeza, O., Pantoja, S. and Kissel, C., 2015. Holocene variations in productivity associated with changes in glacier activity and freshwater flux in the central basin of the Strait of Magellan. Palaeogeography, Palaeoclimatology, Palaeoecology, 436: 112-122.

Auclair, M., Lamothe, M., Huot, S., 2003. Measurement of anomalous fading for feldspar IRSL using SAR. Radiation Measurements, 37: 487-492.

Auer, V., 1959. The Pleistocene of Fuego-Patagonia: Part III: shorelines displacements. Annales Academiae Scientiarum Fennicae, series A, III(60): 1-247.

Balco, G., Stone, J.O., Lifton, N.A., Dunai, T.J., 2008. A complete and easily accessible means of calculating surface exposure ages or erosion rates from 10Be and 26Al measurements. Quaternary geochronology, 3(3): 174-195.

Benn, D. and Evans, D., 1998: Glaciers and Glaciation. Arnold. London.

Bentley, M.J., McCulloch, R.D., 2005. Impact of neotectonics on the record of glacier and sea level fluctuations, Strait of Magellan, southern Chile. Geografiska Annaler, 87 A (2): 393–402.

Bentley, M.J., Sugden, D.E., Hulton, N.R.J., McCulloch, R.D., 2005. The landforms and pattern of deglaciation in the Strait of Magellan and Bahía Inútil, southernmost South America. Geografiska Annaler, 87A(2): 313–333.

Bierman, P.R., Caffee, M.W., Davis, P.T., Marsella, K., Pavich, M., Colgan, P.,Mickelson, D., Larsen, J., 2002. Rates and Timing of Earth Surface Processes from in Situ-produced Cosmogenic Be-10, Beryllium: Mineralogy, Petrology, and Geochemistry. Mineralogical Soc America, Washington, pp. 147-205.

Björck, S., Lambeck, K., Möller, P., Waldmann, N., Bennike, O., Jiang, H., Li, D., Sandgren, P., Nielsen, A.B., Porter, C., 2021. Relative sea level changes and glacio-isostatic modelling in the Beagle Channel, Tierra del Fuego, Chile: glacial and tectonic implications. Quaternary Science Reviews, 251: p.106657.

Blaikie, J., 2020. Palaeoenvironmental reconstruction of Late Glacial-Holocene environmental change for Patagonia, southern South America. Unpublished PhD thesis, University of Stirling, UK.

Bøtter-Jensen, L., Bulur, E., Duller, G.A.T., Murray, A.S., 2000. Advances in luminescence instrument systems. Radiation Measurements, 32: 523-528.

Bøtter-Jensen, L., Andersen, C.E., Duller, G.A.T., Murray, A.S., 2003. Developments in radiation, stimulation and observation facilities in luminescence measurements. Radiation Measurements, 37: 535-541.

Bøtter-Jensen, L., Thomsen, K., Jain, M., 2010. Review of optically stimulated luminescence (OSL) instrumental developments for retrospective dosimetry. Radiation Measurements, 45(3-6): 253-257.

Boyd, B.L., Anderson, J.B., Wellner, J.S., Fernández, R.A., 2008. The sedimentary record of glacial retreat, Marinelli Fjord, Patagonia: Regional correlations and climate ties. Marine Geology, 255(3-4): 165-178.

Caldenius, C.C., 1932. Las glaciaciones cuaternarias en la Patagonia y Tierra del Fuego. Geografiska Annaler, 14: 1–164.

Clapperton, C.M., Sugden, D.E., Kauffman, D., McCulloch, R.D., 1995. The last glaciation in central Magellan Strait, southernmost Chile. Quaternary Research, 44: 133–148.

Cunningham, A.C., Wallinga, J., 2010. Selection of integration time intervals for quartz OSL decay curves. Quaternary Geochronology, 5: 657-666.

Darvill, C.M., Bentley, M.J., Stokes, C.R., 2015. Geomorphology and weathering characteristics of erratic boulder trains on Tierra del Fuego, southernmost South America: implications for dating of glacial deposits. Geomorphology, 228: 382-397.

Davies, B.J., Darvill, C.M., Lovell, H., Bendle, J.M., Dowdeswell, J.A., Fabel, D., García, J-L., Geiger, A., Glasser, N.F., Gheorghiu, D.M., Harrison, S., Hein, A.S., Kaplan, M.R., Martin, J.R.V., Mendelova, M., Palmer, A., Pelto, M., Rodés, Á., Sagredo, E.A., Smedley, R., Smellie, J.L., Thorndycraft, V.R., 2020. The evolution of the Patagonian Ice Sheet from 35 ka to the present day (PATICE). Earth-Science Reviews, 204: 103152.

Dugmore, A.J., Larsen, G., Newton, A.J., Sugden, D.E., 1992. Geochemical stability of finegrained silicic tephra layers in Iceland and Scotland. Journal of Quaternary Science, 7: 173–183.

Evenson, E.B., Burkhart, P.A., Gosse, J.C., Baker, G.S., Jackofsky, D., Meglioli, A., Dalziel, I., Kraus, S., Alley, R.B. and Berti, C., 2009. Enigmatic boulder trains, supraglacial rock avalanches, and the origin of “Darwin's boulders," Tierra del Fuego. GSA Today, 19(12): 4-10.

Eyles, N., Eyles, C.H. and Miall, A.D., 1983: Lithofacies types and vertical profile models, an alternative approach to the description and environmental interpretation of glacial diamict and diamictite sequences. Sedimentology, 30: 393–410.

Fernández, R., Gulick, S., Rodrigo, C., Domack, E., Leventer, A., 2017. Seismic stratigraphy and glacial cycles in the inland passages of the Magallanes Region of Chile, southernmost South America. Marine Geology, 386: 19-31.

Fick, S.E. and Hijmans, R.J., 2017. WorldClim 2: new 1-km spatial resolution climate surfaces for global land areas. International journal of climatology, 37(12): 4302-4315.

Fontana, S. L., Bennett, K., 2012. Postglacial vegetation dynamics of western Tierra del Fuego. The Holocene, 22(11): 1337-1350.

Galbraith, R. F, Roberts, R. G., Laslett, G. M., Yoshida, H., Olley, J. M., 1999, Optical dating of single and multiple grains of quartz from Jinmium rock shelter, northern Australia: Part I, experimental design and statistical models, Archaeometry, 41(2): 339–64.

Garcia, J., Maldonado, A., de Porras, M., Nuevo Delaunay, A., Reyes, O., Ebensperger, C., Binnie, S., Lüthgens, C., Méndez, C., 2019. Early deglaciation and paleolake history of Río Cisnes Glacier, Patagonian Ice Sheet (44°S). Quaternary Research, 91: 194-217.

Guilderson, T.P., Burckle, L., Hemming, S., Peltier, W.R., 2000. Late Pleistocene sea level variations derived from the Argentine Shelf. Geochemistry, Geophysics, Geosystems, 1(12).

Gurdiel, I., Rada, C., Malz, P., Braun, M., Casassa, G., 2022. Glacier inventory and recent variations of Santa Inés Icefield, Southern Patagonia. Arctic, Antarctic, and Alpine Research, 54(1): 202-220.

Hall, B.L., Porter, C.T., Denton, G.H., Lowell, T.V., Bromley, G.R.M., 2013. Extensive recession of Cordillera Darwin glaciers in southernmost South America during Heinrich stadial 1. Quaternary Science Reviews, 62: 49-55.

Hall, B.L., Denton, G., Lowell, T., Bromley, G.R.M., Putnam, A.E., 2017. Retreat of the Cordillera Darwin icefield during Termination I. Cuadernos de Investigación Geográfica, 43(2): 751–766.

Hall, B.L., Lowell, T. V, Bromley, G.R.M., Denton, G.H., Putnam, A.E., 2019. Holocene glacier fluctuations on the northern flank of Cordillera Darwin, southernmost South America. Quaternary Science Reviews, 222: 105904.

Hayward, C., 2012. High spatial resolution electron probe microanalysis of tephras and melt inclusions without beam-induced chemical modification. The Holocene, 22: 119–125.

Hogg, A.G., Heaton, T.J., Hua, Q., Palmer, J.G., Turney, C.S.M., Southon, J., Bayliss, A., Blackwell, P.G., Boswijk, G., Bronk Ramsey, C., Pearson, C., Petchey, F., Reimer, P., Reimer, R., Wacker, L., 2020. SHCal20 southern hemisphere calibration, 0–55,000 years cal BP. Radiocarbon, 62(4): 759–778.

Hunt, J.B. and Hill, P.G., 1993. Tephra geochemistry: a discussion of some persistent analytical problems. The Holocene, 3: 271–278.

Huntley, D., Baril, M., 1997. The K content of the K-feldspars being measured in optical and thermoluminescence dating. Ancient TL ,15: 11-13.

Huntley, D.J., Lamothe, M., 2001. Ubiquity of anomalous fading in K-feldspars and the measurement and correction for it in optical dating. Canadian Journal of Earth Sciences, 38(7): 1093-1106.

Jouzel, J., Masson-Delmotte, V., Cattani, O., Dreyfus, G., Falourd, S., Hoffmann, G., Minster, B., Nouet, J., Barnola, J.M., Chappellaz, J., Fischer, H., 2007. Orbital and millennial Antarctic climate variability over the past 800,000 years. Science, 317(5839): 793-796.

Kaplan, M.R., Coronato, A., Hulton, N.R.J., Rabassa, J.O., Kubik, P.W. and Freeman, S.P.H.T., 2007. Cosmogenic nuclide measurements in southernmost South America and implications for landscape change. Geomorphology, 87(4): 284-301.

Kaplan, M.R., Fogwill, C.J., Sugden, D.E., Hulton, N.R.J., Kubik, P.W., Freeman, S.P.H.T., 2008. Southern Patagonian glacial chronology for the Last Glacial period and implications for Southern Ocean climate. Quaternary Science Reviews, 27(3-4): 284-294.

Kaplan, M.R., Strelin, J.A., Schaefer, J.M., Denton, G.H., Finkel, R.C., Schwartz, R., Putnam, A.E., Vandergoes, M.J., Goehring, B.M., Travis, S.G., 2011. In-situ cosmogenic 10Be production rate at Lago Argentino, Patagonia: implications for late-glacial climate chronology. Earth and Planetary Science Letters, 309(1-2): 21-32.

Kendall, R.A., Mitrovica, J.X., Milne, G.A., 2005. On post-glacial sea level–II. Numerical formulation and comparative results on spherically symmetric models. Geophysical Journal International, 161(3): 679-706.

Kohl, C.P., Nishiizumi, K., 1992., Chemical isolation of quartz for measurement of in situ-produced cosmogenic nuclides. Geochimica et Cosmochimica Acta, 56: 3583-3587.

Krbetschek, M., Götze, J., Dietrich, A., Trautmann, T., 1997. Spectral information from minerals relevant for luminescence dating. Radiation Measurements, 27: 695-748.

Kreutzer, S., Fuchs, M., Meszner, S., Faust, D., 2012. OSL chronostratigraphy of a loess-palaeosol sequence in Saxony/Germany using quartz of different grain sizes. Quaternary Geochronology, 10: 102-109.

Kulig G., 2005. Erstellung einer Auswertesoftware zur Altersbestimmung mittels Lumineszenzverfahren unter spezieller Berücksichtigung des Einflusses radioaktiver Ungleichgewichte in der 238U-Zerfallsreihe. 35 p., B.Sc. thesis, Freiberg (Technische Universität Bergakademie Freiberg).

Lambeck, K., Rouby, H., Purcell, A., Sun, Y., Sambridge, M., 2014. Sea level and global ice volumes from the last glacial maximum to the Holocene. Proceedings of the National Academy of Sciences of the United States of America, 111 (43): 15296-15303.

Lifton, N., Sato, T., Dunai, T. J., 2014. Scaling in situ cosmogenic nuclide production rates using analytical approximations to atmospheric cosmic-ray fluxes. Earth and Planetary Science Letters, 386: 149-160.

Lira, M.P., García, J.L., Bentley, M.J., Jamieson, S.S., Darvill, C.M., Hein, A.S., Fernández, H., Rodés, Á., Fabel, D., Smedley, R.K. and Binnie, S.A., 2022. The last glacial maximum and deglacial history of the Seno Skyring Ice Lobe (52 S), Southern Patagonia. Frontiers in Earth Science, 10, 892316.

Lira, M.P., 2024. Understanding the controls on the extension and the timing of the Patagonian Ice Sheet during the last glacial cycle. Unpublished PhD thesis, University of Durham, UK.

Lüthgens C., Neuhuber S., Grupe S., Payer, T., Peresson. M., Fiebig, M., 2017. Geochronological investigations using a combination of luminescence and cosmogenic nuclide burial dating of drill cores from the Vienna Basin. Zeitschrift der Deutschen Gesellschaft für Geowissenschaften, 168(1): 115-140.

Lüthi, D., Le Floch, M., Bereiter, B., Blunier, T., Barnola, J.M., Siegenthaler, U., Raynaud, D., Jouzel, J., Fischer, H., Kawamura, K., Stocker, T.F., 2008. High-resolution carbon dioxide concentration record 650,000–800,000 years before present. Nature, 453(7193): 379-382.

Mansilla, C.A., 2015. Palaeoenvironmental changes in southern Patagonia during the Late-glacial and the Holocene: implications for forest establishment and climate reconstructions. Unpublished PhD thesis, University of Stirling, UK.

Mansilla, C.A., McCulloch, R.D., Morello, F., 2016. Palaeoenvironmental change in Southern Patagonia during the late glacial and Holocene: Implications for forest refugia and climate reconstructions. Palaeogeography, Palaeoclimatology, Palaeoecology, 447: 1–11.

Mansilla, C.A., McCulloch, R.D., Morello, F., 2018. The vulnerability of the Nothofagus forest-steppe ecotone to climate change: Palaeoecological evidence from Tierra del Fuego (53◦S). Palaegeography, Palaeoclimatology, Palaeoecology, 508: 59–70.

Mark, H.F., Wiens, D.A., Ivins, E.R., Richter, A., Ben Mansour, W., Magnani, M.B., Marderwald, E., Adaros, R., Barrientos, S., 2022. Lithospheric erosion in the Patagonian slab window, and implications for glacial isostasy. Geophysical Research Letters, 49(2): e2021GL096863.

McCulloch, R.D., Bentley, M.J., 1998. Late glacial ice advances in the Estrecho de Magallanes, southern Chile. Quaternary Science Reviews, 17: 775-787.

McCulloch, R.D., Bentley, M.J., Purves, R.S., Hulton, N.R.J., Sugden, D.E., Clapperton, C.M., 2000. Climatic inferences from glacial and palaeoecological evidence at the last glacial termination, southern South America. Journal of Quaternary Science, 15: 409–417.

McCulloch, R.D., Davies, S., 2001. Late-glacial and Holocene palaeoenvironmental change in the Central Strait of Magellan, southern Patagonia. Palaeogeography, Palaeoclimatology, Palaeoecology, 173: 143–173.

McCulloch, R.D., Fogwill, C.J., Sugden, D.E., Bentley, M.J., Kubik, P.W., 2005a. Chronology of the last glaciation in Central Strait of Magellan and Bahía Inútil, southernmost South America. Geografiska Annaler 87A(2): 289–312.

McCulloch, R.D., Bentley, M.J., Tipping, R.M., Clapperton, C.M., 2005b. Evidence for late-glacial ice dammed lakes in the central Strait of Magellan and Bahía Inútil, southernmost South America. Geografiska Annaler, 87A (2), 335–362.

McCulloch, R.D., Blaikie, J., Jacob, B., Mansilla, C.A., Morello, F., De Pol-Holz, R., San Román, M., Tisdall, E., Torres, J., 2020. Late glacial and Holocene climate variability, southernmost Patagonia. Quaternary Science Reviews, 229: 106131.

McCulloch, R.D., Mansilla, C.A., Roberts, S.J., Tisdall, E.W., 2023. Late Quaternary climatic inferences from southern Patagonia (~ 53° S): A holistic palaeoecological approach to tracking the behaviour of the southern westerly winds. Palaeogeography, Palaeoclimatology, Palaeoecology, 631: 111822.

Mejdahl, V., 1979. Thermoluminescence dating: beta attenuation in quartz grains. Achaeometry, 21: 61-73.

Mendoza, L., Perdomo, R., Hormaechea, J.L., Cogliano, D.D., Fritsche, M., Richter, A., Dietrich, R., 2011. Present-day crustal deformation along the Magallanes–Fagnano Fault System in Tierra del Fuego from repeated GPS observations. Geophysical Journal International, 184(3): 1009-1022.

Mercer, J.H., 1976. Glacial history of southernmost South America. Quaternary Research, 6: 125–166.

Milne, G.A. and Mitrovica, J.X., 1998. Postglacial sea-level change on a rotating Earth. Geophysical Journal International, 133(1): 1-19.

Mitrovica, J.X. and Milne, G.A., 2003. On post-glacial sea level: I. General theory. Geophysical Journal International, 154(2): 253-267.

Morello, F., Borrero, L., Massone, M., Stern, C., García-Herbst, A., McCulloch, R., Arroyo-Kalin, M., Calás, E., Torres, J., Prieto, A., Martinez, I., Bahamonde, G., Cárdenas, P., 2012. Hunter-gatherers, biogeographic barriers and the development of human settlement in Tierra del Fuego. Antiquity. Cambridge University Press, 86(331): 71–87.

Moreno, P.I., Lambert, F., Hernández, L. and Villa-Martínez, R.P., 2023. Environmental evolution of western Tierra del Fuego (~ 54° S) since ice-free conditions and its zonal/hemispheric implications. Quaternary Science Reviews, 322: 108387.

Nishiizumi, K., Imamura, M., Caffee, M.W., Southon, J.R., Finkel, R.C., McAninch, J., 2007. Absolute calibration of Be-10 AMS standards. Nuclear Instruments and Methods in Physics Research Section B, 258: 403-413.

NOAA, National Centers for Environmental Information, 2022. ETOPO 2022 15 Arc- Second Global Relief Model. NOAA National Centers for Environmental Information. https://doi.org/10.25921/fd45-gt74. (Accessed 15 July 2024).

Pedro, J.B., Bostock, H.C., Bitz, C.M., He, F., Vandergoes, M.J., Steig, E.J., Chase, B.M., Krause, C.E., Rasmussen, S.O., Markle, B.R., Cortese, G., 2016. The spatial extent and dynamics of the Antarctic Cold Reversal. Nature Geoscience, 9(1): 51-55.

Peltier, C., Kaplan, M.R., Birkel, S.D., Soteres, R.L., Sagredo, E.A., Aravena, J.C., Araos, J., Moreno, P.I., Schwartz, R., Schaefer, J.M., 2021. The large MIS 4 and long MIS 2 glacier maxima on the southern tip of South America. Quaternary Science Reviews, 262: 106858.

Peltier, W.R., Argus, D.F., Drummond, R., 2015. Space geodesy constrains ice age terminal deglaciation: The global ICE-6G_C (VM5a) model. Journal of Geophysical Research: Solid Earth, 120(1): 450-487.

Porter, S.C., Stuiver, M., Heusser, C.J., 1984. Holocene sea level changes along the Strait of Magellan and Beagle Channel, southernmost South America. Quaternary Research, 22: 59-67.

Prescott, J., Stephan, L., 1982. The contribution of cosmic radiation to the environmental dose for thermoluminescent dating - Latitude, altitude and depth dependencies. PACT, 6: 17-25.

Prescott, J., Hutton J., 1994. Cosmic ray distributions to dose rates for luminescence and ESR dating: large depths and long-term variations. Radiation Measurements, 23: 497-500.

Uribe, P., 1982. Deglaciación en el sector central del Estrecho de Magallanes: consideraciones geomorfológicas y cronológicas. Anales del Instituto de la Patagonia, 13: 103-111.

Rades, E.F., Fiebig, M., Lüthgens, C., 2018. Luminescence dating of the Rissian type section in southern Germany as a base for correlation. Quaternary International, 478: 38-50.

Reynhout, S.A., Kaplan, M.R., Sagredo, E.A., Aravena, J.C., Soteres, R.L., Schwartz, R., Schaefer, J.M., 2022. Holocene glacier history of northeastern Cordillera Darwin, southernmost South America (55° S). Quaternary Research, 105: 166-181.

Sagredo, E.A., Moreno, P.I., Villa-Martínez, R., Kaplan, M.R., Kubik, P.W., Stern, C.R., 2011. Fluctuations of the Última Esperanza ice lobe (52◦S), Chilean Patagonia, during the last glacial maximum and termination 1. Geomorphology, 125: 92–108.

Sánchez, A., Pavlishina, P., Godoy, E., Hervé, F., Fanning, C.M., 2010. On the presence of upper Paleocene rocks in the foreland succession at Cabo Nariz, Tierra del Fuego, Chile: geology and new palynological and U–Pb data. Andean Geology, 37: 413–432.

Steffen, R., Wu, P., Steffen, H., Eaton, D.W., 2014. The effect of earth rheology and ice-sheet size on fault slip and magnitude of postglacial earthquakes. Earth and Planetary Science Letters, 388:71-80.

Stern, C.R., 1992. Tefrocronologia de Magallanes: nuevos datos e implicaciones. Anales del Instituto de la Patagonia, 21: 129-141.

Stuiver, M., Reimer, P.J., 1993. Extended ^{14}C database and revised CALIB radiocarbon calibration program. Radiocarbon, 35: 215-230.

Troch, M., Bertrand, S., Lange, C.B., Cardenas, P., Arz, H., Pantoja-Gutiérrez, S., De Pol-Holz, R., Kilian, R., 2022. Glacial isostatic adjustment near the center of the former Patagonian Ice Sheet (48°S) during the last 16.5 kyr. Quaternary Science Reviews, 277: 107346.

Wintle, A.G., 1973. Anomalous Fading of Thermo-luminescence in Mineral Samples. Nature, 245: 143-144.